Exp Fluids (2011) 50:1071–1091
DOI 10.1007/s00348-010-1014-x

RESEARCH ARTICLE

Eulerian and Lagrangian views of a turbulent boundary layer flow using time-resolved tomographic PIV

A. Schröder · R. Geisler · K. Staack · G. E. Elsinga · F. Scarano · B. Wieneke · A. Henning · C. Poelma · J. Westerweel

Received: 16 November 2009 / Revised: 2 November 2010 / Accepted: 17 November 2010 / Published online: 12 December 2010

Abstract Coherent structures and their time evolution in the logarithmic region of a turbulent boundary layer investigated by means of 3D space–time correlations and time-dependent conditional averaging techniques are the focuses of the present paper. Experiments have been performed in the water tunnel at TU Delft measuring the particle motion within a volume of a turbulent boundary layer flow along a flat plate at a free-stream velocity of 0.53 m/s at $Re_\theta = 2{,}460$ based on momentum thickness by using time-resolved tomographic particle image velocimetry (PIV) at 1 kHz sampling rate and particle tracking velocimetry (PTV). The obtained data enable an investigation into the flow structures in a 3D Eulerian reference frame within time durations corresponding to 28 δ/U. An analysis of the time evolution of conditional averages of vorticity components representing inclined hairpin-like legs and of Q2- and Q4-events has been performed, which gives evidence to rethink the early stages of the classical hairpin development model for high Reynolds number TBLs. Furthermore, a PTV algorithm has been applied on the time sequences of reconstructed 3D particle image distributions identifying thousands of particle trajectories that enable the calculation of probability distributions of the three components of Lagrangian accelerations.

Abbreviations

DNS	Direct numerical simulations
HWA	Hot-wire anemometry
LDA	Laser Doppler anemometry
LSE	Linear stochastic estimation
MART	Multiplicative algebraic reconstruction technique
PDF	Probability density function
PIV	Particle image velocimetry

Present Address:
A. Schröder (✉) · R. Geisler · K. Staack · A. Henning
Deutsches Zentrum für Luft- und Raumfahrt,
Institut f. Aerodynamik und Strömungstechnik,
Bunsenstrasse 10, 37073 Göttingen, Germany
e-mail: andreas.schroeder@dlr.de

R. Geisler
e-mail: reinhard.geisler@dlr.de

G. E. Elsinga
Department of Aerospace Engineering,
Delft University of Technology,
Leeghwaterstraat 21, 2628 CA Delft,
The Netherlands
e-mail: g.e.elsinga@tudelft.nl

F. Scarano
Department of Aerospace Engineering,
Delft University of Technology, Kluyverweg 1,
2629 HS Delft, The Netherlands
e-mail: f.scarano@tudelft.nl

B. Wieneke
La Vision GmbH, Anna-Vandenhoeck-Ring 19,
37081 Göttingen, Germany
e-mail: bwieneke@lavision.de

A. Henning
Technical University Berlin, Berlin, Germany

C. Poelma · J. Westerweel
Laboratory for Aero- and Hydrodynamics,
Delft University of Technology, Leeghwaterstraat 21,
2628 CA Delft, The Netherlands
e-mail: c.poelma@tudelft.nl

J. Westerweel
e-mail: j.westerweel@tudelft.nl

ppp	Particles per pixel
PTV	Particle tracking velocimetry
RMS	Root mean square
(T)BL	(Turbulent) boundary layer
TR	Time resolved
WU	Wall units

List of symbols

t	Time
u, v, w	Instantaneous velocity components in x- (streamwise), y- (wall normal) and z-(spanwise) directions
u', v', w'	Fluctuation velocity components
u^+, v^+, w^+	Instantaneous velocity components based on u_τ
x, y, z	Streamwise, wall normal and spanwise coordinates
a_x, a_y, a_z	Components of Lagrangian acceleration
x^+, y^+, z^+	Distances in wall units based on u_τ
k_x, k_y, k_z	Wavenumbers in x-, y- and z-direction
u_τ	Skin friction velocity
η	Kolmogorov length scale
τ_η	Kolomogorov time scale
Re_θ	Reynolds number based on momentum thickness of boundary layer
Re_τ	Reynolds number based on u_τ and δ
c_f	Skin friction coefficient
f	Focal length
$f_\#$	Aperture stop
Q1,…,Q4	Quadrants of instantaneous Reynolds stress $u'v'$
Q, R	Invariants of the velocity gradient tensor
U	Free-stream velocity
δ	Boundary layer thickness ($0.99U_\infty$)
$\delta_0 = 2.6$ mm	(Boundary layer thickness at tripping)
λ_2	Measure of swirl strength (second negative eigenvalue of $S^2 + \Omega^2$)
R_{ij}	Space–(time) correlation function (i and j scalars e.g. u', v' or w')
$k_x\phi_{ij}$	Pre-multiplied cross- or co-spectrum

1 Introduction

The flat-plate turbulent boundary layer (TBL) flow with zero pressure gradients is a canonical wall-bounded turbulent flow that consists of a broad range of temporal and spatial scales of self-organized flow structures, from which some have been identified of playing a major role such as hairpin (-like) vortices, their packets and high- and low-speed streaks. In the past two decades, considerable experimental and numerical work on such coherent structures in wall-bounded turbulent flows has been carried out, e.g. Spalart (1988), Guezennec (1989), Robinson (1991); Schoppa and Hussain (1997); Tomkins and Adrian (2003); Kähler (2004); Hambleton et al. (2006), del Alamo et al. (2006), Hutchins and Marusic (2007); Adrian (2007); Herpin et al. (2008); Stanislas et al. (2008), Schlatter et al. (2010). A review and analysis of numerical and experimental data on wall-bounded turbulence has been composed very recently by Marusic et al. (2010). But still questions remain on the mechanisms for the exchange of momentum and energy of the TBL flow between the large-scale motions down to the smallest eddies leading to viscous dissipation and the role of the coherent structures for the inertial and dissipative regime. Furthermore, the Reynolds number effects on the specific topologies and coherent structure organization are still under discussion, especially because DNS on TBL's with an established logarithmic region are available just since a few years. Therefore, the present paper is focused on the investigation into coherent structures, especially those related to the negative Reynolds stress events (Q2 and Q4) within the logarithmic region of the TBL flow. At the present boundary layer profile, a logarithmic layer is present with a typical slope for this Reynolds number (see Fig. 2).

Over almost two decades, the PIV technique has enabled the determination of two-component and later on three-component instantaneous velocity vector fields in one plane of the flow, delivering important topological results based on instantaneous and statistical approaches to the analysis of the turbulent flow structures. Extensions of PIV towards dual-plane measurements and/or time-resolved measurements have been performed in the recent years, whereby their application to turbulent flows has further emphasized the role of coherent structures in this research field. In a recent paper, Stanislas et al. (2008) describe the scaling properties, topologies and distribution functions of vortices in a turbulent boundary layer for two different Reynolds numbers at $Re_\theta = 7{,}800$ and $Re_\theta = 15{,}000$ on the basis of PIV results by using e.g. conditional averaging (LSE–linear stochastic estimation) and spatial correlation. They found that fully developed hairpin vortices in high Reynolds number flows appear dominantly one-sided and cane-shaped. Furthermore, a region of strong interaction between vortices in the region of $y^+ < 150$ can be distinguished from a region $y^+ > 150$ where these interactions are less often. Another focus of investigation was the relation of streamwise vorticity, low-momentum streaks and negative Reynolds stress events by LSE in the spanwise wall normal plane assuming a classical hairpin model with a streamwise-oriented vortex axis accompanying the near-wall low-speed streaks. However, recently, a costly high Reynolds number DNS and LES of spatially fully developed TBL flow calculated on 8×10^9 grid points from Schlatter et al. (2010) show in a poster representation

of Schlatter (2010) that the presence of classic symmetrical hairpin structures seems to be a transitional and low Reynolds number effect, while at higher $Re_\theta > 2{,}500$, these vortices became rare: In this simulation, the dominant vortical structures in the fully developed logarithmic region are inclined, mostly one-sided and formed as a cane or an arch. Furthermore, the numerical data show streaky structures of low- and high-momentum fluid persisting with different scaling properties from the near-wall region through the whole boundary layer up to the wake region.

The observation that quasi-streamwise-oriented vortices (the correlation of positive v' and negative u' et vice versa along wall-bounded streaks) seem to be a secondary process due to an interaction of high-momentum 'sweeps' with low-speed streaks, while stronger x-vorticity events have only relatively short streamwise extensions at $Re_\theta = 7{,}800$ and 15,000 has been made on the basis of dual-plane and Stereo PIV measurements by Kähler (2004). This observation will play a role later in the paper. Nevertheless, all studies agree that vortices play a major role in the spatial organization of wall-normal and spanwise momentum exchange. They are apparently connected to the turbulence production events, the (instantaneous) negative Reynolds stresses $u'v'$, so-called Q2 and Q4-events in the buffer and log layer.

In a double-field SPIV set-up, Foucaut et al. (2010) constructed 3D two-point correlation functions for u', v', w' and $u'v'$ in a TBL at $Re_\theta = 9{,}800$. Form and orientation of the 3D correlation functions are similar to what can be found in the literature and the present investigation. Ganapathisubramani et al. (2005) calculated two-point correlation functions from SPIV measurements in three different planes crossing the logarithmic region of a TBL at $Re_\tau = 1{,}100$. One plane was oriented in spanwise–streamwise direction, and two other planes were inclined by 45° and 135° towards the wall. A quasi-3D representation of R_{ij} using all three components of velocity fluctuation was possible in that way confirming that average wall normal motion is connected to low-momentum fields. They assume the presence of packets of hairpins to be responsible for that correspondence. Diorio et al. (2007) report results of multiple hot-wire measurements in a TBL. The data enable them to reconstruct the average spatial neighbourhood of dissipation and production regions. They claim to have identified the highest instantaneous dissipation rates within the vortex lines of, for example, a hairpin leg, while the highest production rates are located in both spanwise vicinities as Q2 and Q4 events. In the results chapter of the present paper, time-dependent conditional averaging of our data at Q2- and Q4-events and one sign of y-vorticity will provide a generic 3D topology of the development of these neighbourhood relations (see Figs. 8, 9).

Recently, Elsinga et al. (2007) report on the application of tomographic PIV to a tripped turbulent boundary layer flow at a low Reynolds number. In this paper, instantaneous spatial topologies of the coherent structures like hairpin vortices, packets of hairpins along low-speed streaks and Q2-events have been visualized segmented in 3D quantitatively. The coherent structures have been extensively described, and global statistics have been calculated for comparison with theory and literature. A very recent investigation of a TBL flow at $Re_\tau = 2{,}400$ has been established by Gao et al. (2010) using snapshot Tomo PIV. They visualized low-speed regions and the vicinity of hairpin-like structures and calculated statistics on vortex inclination angles, diameters and circulation. The first results of time-resolved 3D–3C velocity vector fields from turbulent wall-bounded flows in air gained from tomographic PIV were published by Schröder et al. (2006), also (2008).

The turbulent mixing due to the Q2- and Q4-events in different turbulent boundary layer scenarios has been found to be connected to a staggered pattern of hairpin-like vortices; see the idealized mixer-model of substructure formation inside a turbulent spot of Schröder and Kompenhans (2004) or in a TBL flow of Elsinga et al. (2007). The work of Schröder (2001) on turbulent spots, which represents a self-similar growing mechanism of structures in a low Reynolds number by-pass transition scenario, led to an interpretation of spatial distributions of space–time correlations of the single Reynolds stress elements calculated for different planes parallel to the wall: Here, the initial process for the formation of hairpin vortices seemed to be a Q4-event, which was deflected by a large flow structure of low relative velocity and (sometimes transformed into a Q3 event) guided with spanwise flow variance towards a wall-near low-speed streak. Such events have been found in the 3D–3C and time-resolved data of Schröder et al. (2008), but could not be confirmed yet as an essential mechanism for TBLs.

A study on the evolution and lifetime of the energy-containing eddies based on conditional averaging, the rate of change field of the invariants of the velocity gradient tensor Q and R has been established on the data set presented in this paper for the region between $88 < y^+ < 240$ by Elsinga and Marusic (2010). The study enables the reconstruction of mean orbital trajectories spiralling inside the joint PDF of Q and R, which established an estimation of the characteristic life cycle time of the eddies in the outer logarithmic region of the present TBL to be around ~ 1 s, corresponding to $14.3\delta/U$ or $470\nu/u_\tau^2$. In the recent years, special attention has been paid on very long structures of low-momentum fluid in the logarithmic region of TBL flows of sufficiently high Reynolds numbers (e.g. Tomkins and Adrian 2003, Hutchins and Marusic 2007, del Alamo et al. 2006). A detached region of long low-momentum structures which seem to have a topology like a "wake region" behind large vortical events which transport low-momentum fluid away from the wall have been reported by

DNS from del Alamo et al. (2006) and by dual-plane SPIV by Hambleton et al. (2006). The latter ones explain the widening of the "wake" by the meandering nature of the low-speed streaks. Hutchins and Marusic (2007) confirmed these limitations of one-point statistics and gave an estimation of the typical length of such 'superstructures' in the order of $\sim$10–20δ. They are forming, besides the well-known streaks close to the wall, a second peak in the pre-multiplied energy spectrum of the streamwise velocity fluctuation. Most recently, a well-resolved LES calculation with fully spatial development up to $Re_\theta = 4{,}300$ (Schlatter et al. 2010), which has been validated with own DNS data up to $Re_\theta = 2{,}500$, has confirmed these structures forming also a second peak with a spanwise wavelength for u' at about 1.0δ, which corresponds to an average spacing between high- and low-momentum fluid of $\Delta z \sim 0.5\delta$, with a maximum at an average height of $y = 0.35\delta$.

A review on Taylor's hypothesis and problems occurring when using it especially in TBL's due to observed bi-modal effects in the spectrum has been given by Moin (2009). He reports on recent investigations on adapting the dependency of the local convection velocity from the distance to the wall and the eddy wavelength of the convecting structure, which has been reported by Krogstad et al. (1998). In a numerical work from del Alamo and Jiménez (2009), they found that only the smallest eddies follow the local mean and provide a semi-empiric law for pointwise measurement techniques like HWA or LDA that counts for the deviation effects of different wavelength and s.c. global modes, which convect by approximately the bulk velocity. Nevertheless, a precise validity check of Taylor's hypothesis following the trajectories of single-flow structures would require time-dependent 3D data on a huge spatial and temporal domain, which would enable the analysis of the pseudo-Lagrangian motions of all eddy scales, components and topologies within the meandering nature of the spanwise variances of streaky low- and high-momentum fluid regions.

In the past decades, most experimental approaches to TBL flows using particle image velocimetry (PIV), laser Doppler anemometry (LDA) or hot-wire probe techniques led to results within an Eulerian reference frame. The corresponding data led to concepts and models of coherent structures as the main carriers of turbulent mass, momentum and energy exchange. Within a Lagrangian frame of reference, experimental turbulence characterization has been performed mainly by statistical analysis over several spatially independent particles, either single or in groups, measured by tracking methods based on photogrammetric particle tracking velocimetry (Virant and Dracos 1997; Mordant et al. 2009). Only few papers are available dealing with investigations into Lagrangian motions and accelerations in TBL or channel flows using DNS (e.g. Lee et al. (2004), Lavezzo et al. (2009), Yeo et al. (2010)), all of them at relatively low Re_τ between 180 and 600, and even less using experimental methods (e.g. Gerashchenko et al. (2008)). Choi et al. (2004) and Lee et al. (2004) investigated the nature of intermittency of the Lagrangian accelerations especially in near-wall regions of the TBL. They found strong anisotropies for the x- and y-component for $y^+ < 30$ and related both to the presence of the wall and high- and low-speed streaks, while the intermittency is explained by trapping of fluid particles in quasi-streamwise vortices of hairpin type. Here, the acceleration is always normal to the vortex axis, which can be easily explained by centripetal forces. Unfortunately, the logarithmic region was not fully developed in these numerical data and if so, in first signs at $Re_\tau = 600$, only few global statistics are available. Gerashchenko et al. (2008) describes a polydispersed inertial particle motion experiment using PTV in a turbulent channel flow generated by an (active) grid also at relatively low Reynolds numbers with respect to momentum thickness of $Re_\theta = 840$ and 725. Results of the lowest Stokes number case of 0.035 on Lagrangian accelerations might serve as a basis for comparisons with the data from our work. Both DNS and experimental data show that for the integral of the logarithmic region investigated almost similar RMS values are present for the three components of the Lagrangian acceleration and the skewness of these PDFs tends to zero.

Using the PTV technique for detecting Lagrangian motions directly from particle images, the achieved spatial resolution precluded a simultaneous description of the coherent structures. One of the main challenges of experimental turbulence research is therefore the combination of both viewpoints in a single experiment. Of course complete direct numerical simulations (DNS) and specific research topics like particle dispersion in boundary layers, two-phase flows etc. sometimes bridge both reference frames, but up to now no measurement technique was available that enables the capture of both properties of the flow field at the same time.

A focus for a direct comparison of the results of the present work will be the spatio-temporal models of coherent flow structures in the literature, which have been developed partly by using the PIV technique. It will be shown that the data set acquired by time-resolved tomographic PIV over a time duration of 2 s each in the presented work gives valuable insight into the four-dimensional flow organization and exchange mechanisms of coherent flow structures inside a fully developed flat-plate turbulent boundary layer with zero pressure gradients at $Re_\theta = 2{,}460$. We can obtain a description of the fluid motion in both Eulerian and Lagrangian frames of reference from the same high image density experimental data. A topological analysis by means of 3D space–(time) correlations, PDFs of different scalars, time-dependent conditional averaging and time series of instantaneous velocity

vector volumes are the results presented in this paper. Furthermore, probability distributions of Lagrangian accelerations and a view of particle tracks will be shown. On the one hand, the calculation of Lagrangian time scales towards integral values is limited by the finite extent of the measurement volume and the restrictions of the PTV algorithm in finding long-particle trajectories. On the other hand, the very high temporal sampling rate allows a full temporal resolution of the fluid motion down to the Kolmogorov time scale τ_η, which has been estimated from the complete instantaneous velocity gradient tensor from the present data averaged over all samples and planes of constant wall distance between $60 < y^+ < 320$ to be between $\tau_\eta = 25$–44 ms, depending on y-position. This values might be overestimated ($\sim$at least by a factor of 2) due to the strong influence of correlation window size filtering on the spatial derivatives. Following a tomographic reconstruction of a time series of particle image recordings in a volume, a PTV algorithm was employed, enabling a description of the motion of several thousands of particles in a Lagrangian frame of reference within the measurement volume. This approach allows the calculation of the probability distributions of Lagrangian accelerations.

For the Eulerian case, time series of instantaneous 3D velocity vector fields were determined, while the three-dimensional distribution of the vorticity and λ_2 fields are represented as iso-surfaces, which highlight the topology of individual vortical substructures, their evolution in time and the induced flow. Here, λ_2 is the negative of the locally computed eigenvalues of the velocity gradient tensor decomposed into strain and spin and squared ($S^2 + \Omega^2$), which is a measure for rotation excluding shear vorticity (Zhou et al. 1999). It has to be mentioned that the relatively coarse spatial resolution for the buffer and log-layer region in the measurement volume enables only the representation of vortical structures above a certain spatial extension. Nevertheless, the main topologies such as hairpin-like vortices and streaky low- and high-speed regions have been sufficiently resolved.

This paper is organized as follows: Sect. 2 describes the details of the experimental set-up and the measurement procedure. Section 3 is divided in 7 subsections and specifies the results and important flow events by various statistical analyses (TBL profiles, spectra, PDFs and space–time correlations) and a description of flow structures within an instantaneous velocity vector volume. Time-dependent conditional averages of vortices, Q2- and Q4-events presented in Sect. 3.6 enable an interpretation of the history of prominent turbulence producing eddies. Section 3.7 is dedicated to results of the PTV technique showing Lagrangian accelerations. In Sect. 4, a conclusion of the performed work and presented results is drawn.

2 Experimental set-up and procedure

The experiments have been conducted in the water tunnel at TU Delft where a turbulent boundary layer flow has been established along a vertically mounted flat acrylic glass plate at a free-stream velocity of 0.53 m/s. The plate dimensions are 250×80 cm^2, and an elliptic leading edge was employed, while a nearly zero pressure gradient was achieved by adjusting a trailing-edge flap (see sketch in Fig. 1). The flow on the observation side was tripped by a spanwise attached zig-zag band 150 mm downstream of the leading edge. A thickness of the turbulent boundary layer of 38 mm was reached at the location of the measurement volume around its centre at $x = 2{,}090$ mm downstream the leading edge. This corresponds to $Re_\theta = 2{,}460$ based on the momentum thickness and free-stream velocity. The zig-zag band tripping with 1.8 mm height from the wall and resulting downstream flow structures were special topics of an investigation using tomo PIV by Elsinga and Westerweel (2010). They showed a flow separation region and undulated spanwise vortices in the shear layer leading to arch- and hairpin-type vortices. They concluded that these transitional structures no longer affect the turbulent boundary layer flow organization $\sim 500\ \delta_0$ downstream of the trip, with $\delta_0 = 2.6$ mm height of the boundary layer at tripping position. The temperature during the measurement was kept constant, while the turbulence level of the free-stream velocity was below 0.5%. For the general characterization of the boundary layer flow, a $f = 105$ mm lens from *Nikon* was used for a high-resolution 2C-PIV measurement with a low-repetition rate system composed of a *Big Sky CFR-200* laser delivering 200 mJ/pulse energy and a *LaVision Imager PRO-X* camera with a 4 Mpixel sensor. One thousand statistically independent double-frame images in a region of $\sim 50 \times 50$ mm^2 were evaluated using 16×16 pixel interrogation windows, corresponding to a spatial resolution of 8.8 wall units (WU) in the x- (streamwise) and y-(wall normal) direction. These data were used to compute profiles of the mean velocity and root-mean-square fluctuating velocity across the boundary layer. The resulting semi-logarithmic boundary layer profile scaled with wall units, after applying the Clauser method (Clauser (1956)) for the estimation of the skin friction velocity is given in Fig. 2 (left). The skin friction velocity was estimated at $u_\tau = 0.0219$ m/s by means of regression of $u^+ = 1/\kappa * \ln y^+ + C$, where $\kappa = 0.41$, $C = 5.0$, between $y^+ = 44$ and $y^+ = 200$, and corresponds to a friction coefficient of $c_f = 0.00345$. This value is in good agreement with the DNS data from Schlatter et al. (2010) at $Re_\theta = 2{,}400$ of $c_f = 0.00338$. The buffer layer, log-layer and bulk region can be distinguished in the semi-log plot of the profile,

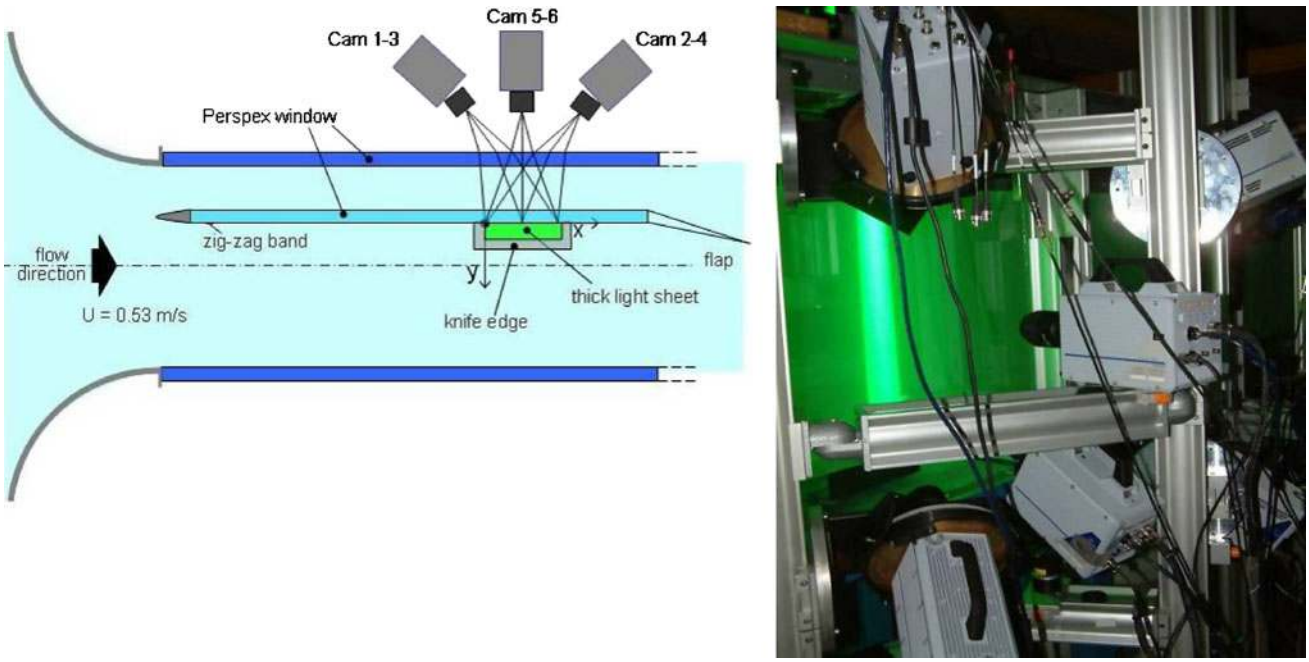

Fig. 1 Six CMOS cameras operating at 1 kHz framing rates in a solid angle view at TU Delft water tunnel. The measurement volume of 63 × 15 × 68 mm^3 was located in a flat-plate TBL flow 2.09 m downstream of the leading edge (see sketch *left*). Photography of set-up and laser illumination of particles at TU Delft water tunnel (*right*)

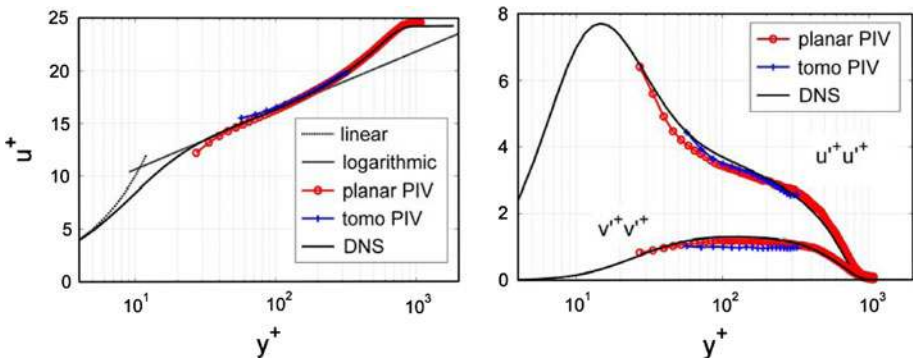

Fig. 2 Mean velocity profile of the turbulent boundary layer at $Re_\theta = 2{,}460$ (*left*) and Reynolds normal stress profiles (*right*) obtained by planar PIV (*red circles*) and tomographic PIV (*blue lines*). For comparison, the corresponding profiles of DNS data at $Re_\theta = 2{,}400$, provided by Schlatter (2010), are presented (*black*)

although the linear viscous sub-layer region (for $y^+ < 10$) could not be resolved sufficiently.

In a second step, a high-repetition rate tomographic PIV system was applied by making use of a diode-pumped double-cavity Nd:YLF laser with a high-repetition rate (*Quantronix*), with a pulse energy of 25 mJ at 1 kHz, and six *Photron* CMOS cameras with 1,024 × 1,024 pixels in full-frame mode (see Fig. 1, left). Five cameras were positioned in an angular viewing geometry with Scheimpflug mounts, while one camera sensor was aligned with its optical axis normal to the mean flow. The volume illumination in a rectangular shape with a nearly homogenous light intensity distribution was provided by guiding the laser beam through two spherical lenses ($f = -100$ and $f = 200$ mm) for expanding and collimating the laser light beam and two cylindrical lenses ($f = -90$ mm and $f = 300$ mm) for beam expanding in one direction. This order of lenses shapes an elliptically extended and collimated beam which has been restricted at the areas of highest intensities using a final knife-edge frame. The light was introduced in spanwise direction, parallel to the plate and perpendicular to the mean flow direction. Since sufficient light was scattered by the polyamide seeding particles with a mean diameter of 56 μm, large optical aberrations due to astigmatism from angular viewing through surfaces of different refractive indices could be avoided by reducing the aperture of the four *Zeiss* $f = 100$ mm and two *Nikon* $f = 105$ mm camera lenses down to $f_\# = 11$. We thus avoided the use of prisms. A volume of about 63 × 15 × 68 mm^3 = 734 × 176 × 793 voxels = 1.65 × 0.4 × 1.79 δ^3 = 1,380 × 328 × 1,490 cubic wall units (WU)^3 in *x*-, *y*- and *z*-direction, respectively (where *x* is in the streamwise direction and y in

the wall normal direction) centred 2,090 mm downstream of the plate leading edge was illuminated at 1 kHz frequency, which is at the same time the PIV sampling frequency. Five sequences of 2,040 images were captured during a period of 2 s. The system was synchronized with a Programmable Timing Unit (*LaVision* PTU9) controlled by *DaVis7.3* software. With the same software tool, the reconstruction of the three-dimensional particle light intensity distributions was computed by means of the MART tomographic algorithm specialized for PIV signals (Elsinga et al. 2006). This returns a 3D array of voxels where the intensity of the light scattered by the particles is stored digitally. Before final reconstruction of the particle image volumes, a volume self-calibration described by Wieneke (2007) was performed. This procedure is required in order to enhance the accuracy of the iterative MART algorithm, resulting in an improved particle reconstruction performance and a reduction in ghost particles. The particle image volume is analysed by local 3D cross-correlations with an iterative multi-grid volume deformation scheme reaching a final 32^3 voxel interrogation box size. For particle image cross-correlation, the time delay Δt between two reconstructed volumes was chosen to be 2 ms in order to enhance the dynamic range for measuring the velocity fluctuations and reduce the number of correlated ghost particles (when evaluating all samples with 50% overlap in time). Due to shear movements inside the flow, ghosts become uncorrelated for larger time delays between two reconstructed subsequent particle volumes (Elsinga et al. 2010). The presence of ghost particles is a statistical result of the MART algorithm, and for a given seeding density, (here about 0.05 ppp) their probability of appearance decreases with the number of cameras viewing from different angles. The relation of ghost to reconstructed real particles was 1–3 in the worst case close to the borders of the reconstructed volumes, which enables a high-quality 3D cross-correlation with less than $\sim$1% outliers per instantaneous vector volume using 32^3 voxel final interrogation volume size. With a given magnification of 85.9 μm/voxel, the final 32^3 voxel volume corresponds to a spatial resolution of $\sim 2.75 \times 2.75 \times 2.75$ mm^3, corresponding to 59.7 WU, and with 75% overlap between adjacent interrogation volumes a series of instantaneous three-dimensional velocity vector volumes over a grid of $92 \times 99 \times 22$ (200,376) measurement points located every 0.687 mm ($\sim$15 WU) in all directions in space for each time step of 2 ms increment were obtained. The under-sampling of vortex structures especially close to the wall when using 59.7 WU interrogation volume size is problematic in the present data, but at regions $y^+ > 60$, the vortex distances are mostly sufficient for a correct representation of the vortex axis, position and shape, even when the vorticity magnitude is underestimated (Tables 1, 2).

Table 1 Basic fluid mechanical properties of the TBL, as estimated by PIV

Reynolds number (Re_θ/Re_τ)	2460/800
Free-stream velocity (U)	0.53 m/s
Friction coefficient (C_f)	0.00345
Friction velocity(u_τ)	0.0219 m/s
Boundary-layer thickness (δ)	38.1 mm
Kolmogorov length scales (η)	$\sim$166–212 μm
Kolmogorov time scales (τ_η)	$\sim$25–44 ms

Table 2 Parameters of final interrogation window (IW) and step size for TomoPIV evaluation and extension of measurement volume in wall units (WU) in flow-, wall normal- and spanwise (x-, y- and z-) directions

IW (WU)	IW step (WU)	x- (WU)	y- (WU)	z- (WU)
59.7	14.9	1,380	328	1,490

3 Results

3.1 Boundary layer statistics

The flow statistics measured by planar and tomographic PIV are presented in Fig. 2. The planar PIV mean velocity profile (Fig. 2 left) reveals the logarithmic layer and wake region as expected. The profile for the tomographic PIV data, however, does not follow the logarithmic profile neither exactly in the slope nor in the points closest to the wall, which can be explained either by an bias shift due to correlated ghosts in the close wall region or an systematic error in the mean local velocity of about 7% estimated from the deviation to the DNS, which might be caused by the filtering effect of the interrogation window size in this region of strong shear. Also, the fact that the Clauser method has been applied on the planar PIV data only for estimating the skin friction velocity plays a role in this deviation. Points within $y^+ < 60$ will consequently not be included in the further analysis below.

The differences in the fluctuating velocity between the techniques, expressed by the Reynolds normal stress profiles (Fig. 2 right), are of sub-pixel order, which is consistent with previous comparisons in cylinder wake flow and turbulent boundary layers (Elsinga 2008; Scarano and Poelma 2009). Nevertheless, some more explanation on the systematic deviation compared to DNS can be given. The window filtering error source has to be considered here on one side. Saikrishnan et al. (2006) considered the effect of spatial resolution on RMS values in boundary layers using dual-plane PIV and DNS data and found that a filtering size of 40 viscous units at $y^+ = 110$ yielded about a 5% underestimation of the RMS of u. For both displayed Reynolds normal stresses in Fig. 2 (right), the underestimation in the

regions $y^+ < 200$ and the overestimation in the regions $y^+ > 200$ can be explained to be an addition of sub-pixel inaccuracies minus the underestimation due to windows filtering, which acts stronger in regions where small-scale eddies are present. Elsinga and Marusic (2010) calculated the filtering effect of 50 WU in each direction for the outer part of the log-layer of a TBL at a similar Reynolds number between $88 < y^+ < 240$ on DNS data and received still 98% of the Reynolds stresses. Furthermore, velocity time series from the highly time-resolved measurement are compared with previous hot-wire measurements in literature to assess the spatial resolution. Applying Taylor's hypothesis with the local average velocity as the convective velocity, pre-multiplied u-spectra $k_x\phi_{uu}$ and the uv-co-spectra $k_x\phi_{uv}$ can be computed (Fig. 3). The areas under these graphs represent the streamwise kinetic energy and the Reynolds shear stress respectively at $y^+ = 120$. The present data compare well with the hot-wire measurements of Nickels and Marusic (2001), indicating that the energy-containing scales of motion have been adequately resolved. However, a small deviation may be noticed near the cut-off wavelength (taken as twice the cross-correlation volume size; 120 WU), which is indicated by the grey dashed line in the Fig. 3. Clearly, the smallest, dissipative scales are modulated due to insufficient spatial resolution. This is also evident from the pre-multiplied spectra $k_x^3\phi_{uu}$, which show the streamwise velocity gradient u_x energy distribution over the wave numbers. Nevertheless, approximately 85% of the total energy in u_x from the reference hot-wire data is still captured in the present tomographic PIV experiment. This can be seen in Fig. 3 as the areas under the respective pre-multiplied spectra overlapping by 85%, where the hotwire reveals additional energy at the smaller scales (high wave number).

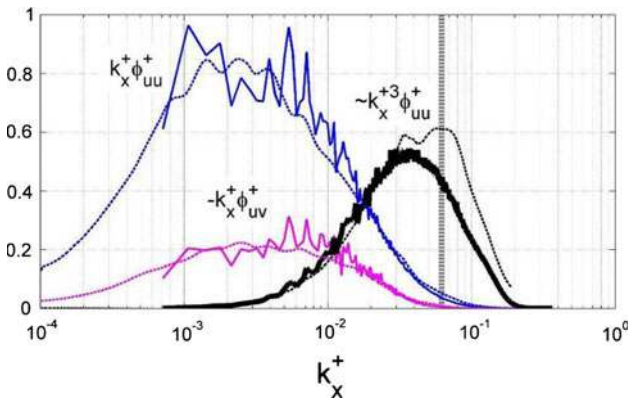

Fig. 3 Pre-multiplied cross- spectra and co-spectra at $y^+ = 120$ comparing tomographic PIV results (*solid lines*) with the profiles reported in Nickels and Marusic (2001) for $Re_\theta = 2730$. The present spatial resolution, defined as twice the correlation volume size, is indicated by the *vertical dashed line*

On the low wave number end, the present measurement is limited due to restrictions in data handling, which meant we could only measure for 2 s corresponding to "only" $\sim 20\delta$ considering $0.75U$ as bulk resp. convection velocity. Still, this allows us to see (part of) the so-called 'superstructures' (Hutchins and Marusic 2007) of long low-momentum fluid zones.

3.2 Instantaneous 3D–3C(t) velocity vector fields

Processing of 10200 tomographic particle volume reconstructions by MART and local 3D cross-correlations of 5100 (each second pair) was carried out on an 8 times dual-core 64-bit cluster using DaVis 7.3. Instantaneous velocity vector volumes with a mean particle image shift of ~ 9 voxels were computed and, after conversion to physical quantities, 3D vorticity and λ_2 (Zhou et al. 1999), as well as the overall velocity average over all 5100 samples, were determined. The number of spurious vectors was less than 1%. For the single instantaneous velocity vector plots, an uncertainty of about ~ 2–3% has to be accepted, because a sub-voxel accuracy of the peak detection of ~ 0.2 pixels is present due to anisotropic intensity distributions of the tomographically reconstructed particles. The accuracy value of ~ 0.2 pixels is a conservative estimation with respect to Elsinga et al. 2006 who showed experimental values between 0.1–0.16 pixels. After subtracting the mean from the single instantaneous velocity vector volumes, the fields of fluctuation velocities u', v' and w' and the four quadrants of the Reynolds stress Q1 to Q4 have been derived. Examples of the results of global and local statistics are shown in the next chapters.

The 4D data with close to 200.000 instantaneous velocity vectors for each volume measured with 1 kHz over 2 s each provide important information about the flow structure development and spatio-temporal distribution of many significant flow events in this relatively low Reynolds number TBL. Such data sets have been found lacking so far in previous investigations of wall-bounded turbulent flows. Especially the relatively long-time sequences of time-resolved data of $\sim 28\delta$/U enable the view on very large-scale meandering motion of the low- and high-momentum streaks in the log layer (e.g. Hutchins and Marusic 2007) of the present data. A further analysis of these structures should be part of future work. Due to the limitations of the spatial resolution close to the wall, we consider only data $y^+ > 60$ for statistical and topological interpretation in the further analysis.

In Fig. 4, a snapshot from the time series of velocity vector volumes shows the distribution of vortical structures shaped as arch (A), one-sided hairpin leg (B), cane (C) or arbitrarily shaped (D) vortices within the turbulent flow, as visualized by the iso-surfaces of the swirl-strength λ_2. Type B and C are of course similar, while B is exceeding the

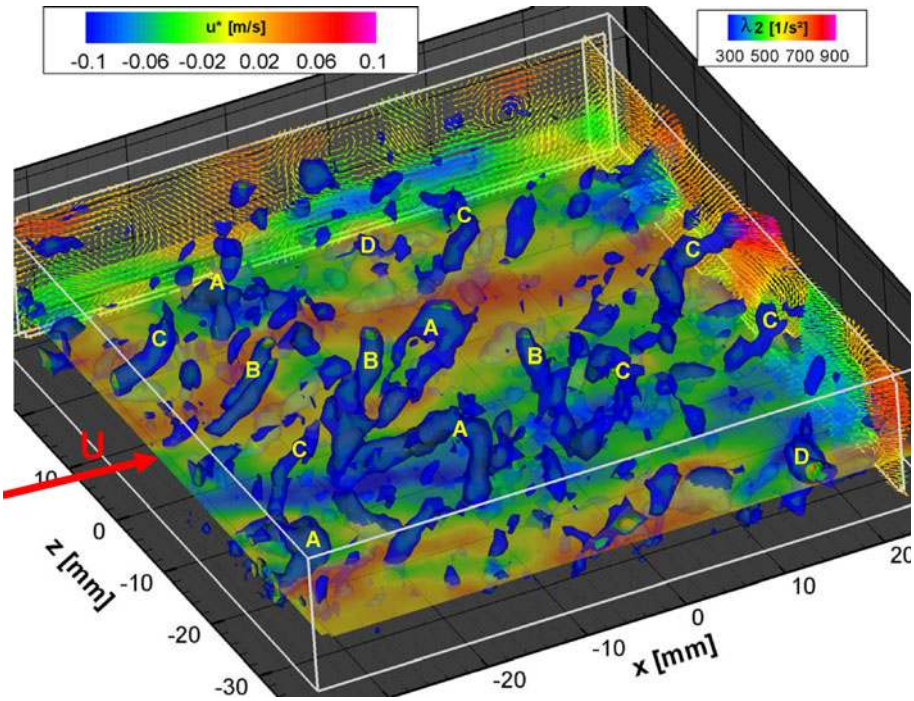

Fig. 4 An instantaneous 3D velocity volume extracted from a time series depicting flow structures by iso-surfaces of swirl-strength value λ_2 (*blue structures*) and selected velocity planes, one stream- and spanwise plane at $y^+ \sim 75$ ($u^* = u - u_{\mathrm{ref}}$ colour coded, $U = 0.53$ m/s)

whole measured y-domain. The colour coding of the vector and contour planes represents the velocities, indicating low- and high-momentum fluid regions. It is visible by the distribution of λ_2 iso-contour surfaces that streak with lower velocity (blue areas in wall-parallel plane) are closely surrounded by different vortical structures (see Adrian (2007), Tomkins and Adrian (2003)) mostly one-sided inclined or cane vortex legs, while the smaller vortices (most of them are not sufficiently resolved) are closer to the wall. Schlatter (2010) found streaky regions of low-momentum fluid penetrating the whole boundary layer thickness, which are organized through merging in growing scales at increasing wall distances. One finding of former investigations (e.g., Kähler 2004) is that the (near-wall) streaky structures are the most important shear generating and by a basic Kelvin–Helmholtz instability also vorticity-generating structures in wall-bounded flows. Nevertheless, most of the vortical structures in our data remain stable over longer times while convecting and meandering downstream along the above-mentioned low-momentum streaks. They increase slightly in height, while canes induce sometimes a "counter rotating vortex leg" on the opposite side of a low-momentum fluid streak, but often at a slightly different streamwise position. New arch or cane-shaped vortices are seldom observed to be created and are located lateral to low-momentum streaks, while a shift and meandering of the streaks can in most cases be connected to strong single-sided inclined cane vortices in our data set. In some cases, very long low-speed streaks are formed by (or connected to) packages of successive arch and cane vortices, as described in PIV results from Christensen and Adrian (2001), Tomkins and Adrian (2003) and Ganapathisubramani et al. (2003). An extensive phenomenological study of the time evolution of the flow structures visualized by quantitative volumetric vector- and iso-surfaces data gives an indication of the huge variety of flow structures present in the flow, from which some are not well known or have so far only been "detected" by visual inspection. A topological analysis by space–time correlations and time-dependent conditional averaging is one necessary step for a more general analysis of the temporal behaviour of coherent flow structures.

3.3 PDFs of the velocity components

For a global statistical view, the PDFs of the velocity and vorticity components–the latter determined by central difference schemes–can give a quick overview of the fluctuations present in the logarithmic layer of this TBL flow. Skewness and shoulders visible in the PDF of u, v and w calculated over 5100 samples of the whole domain between $y^+ = 60$ and 300 shown in Fig. 5 indicate how the velocity fluctuations are distributed, especially for the low- and high-momentum streamwise-elongated structures (Tomkins and Adrian (2003), Hutchins and Marusic (2007)), which are the most important large-scale structures in the log layer of the TBL, which do not convect with the local mean. Schlatter (2010) shows a spatial connection to the similar and well-known high- and low-speed streaks in the near-wall region. Note that we calculated the instantaneous velocity distributions and not the fluctuations. However, the shoulders in the present PDFs

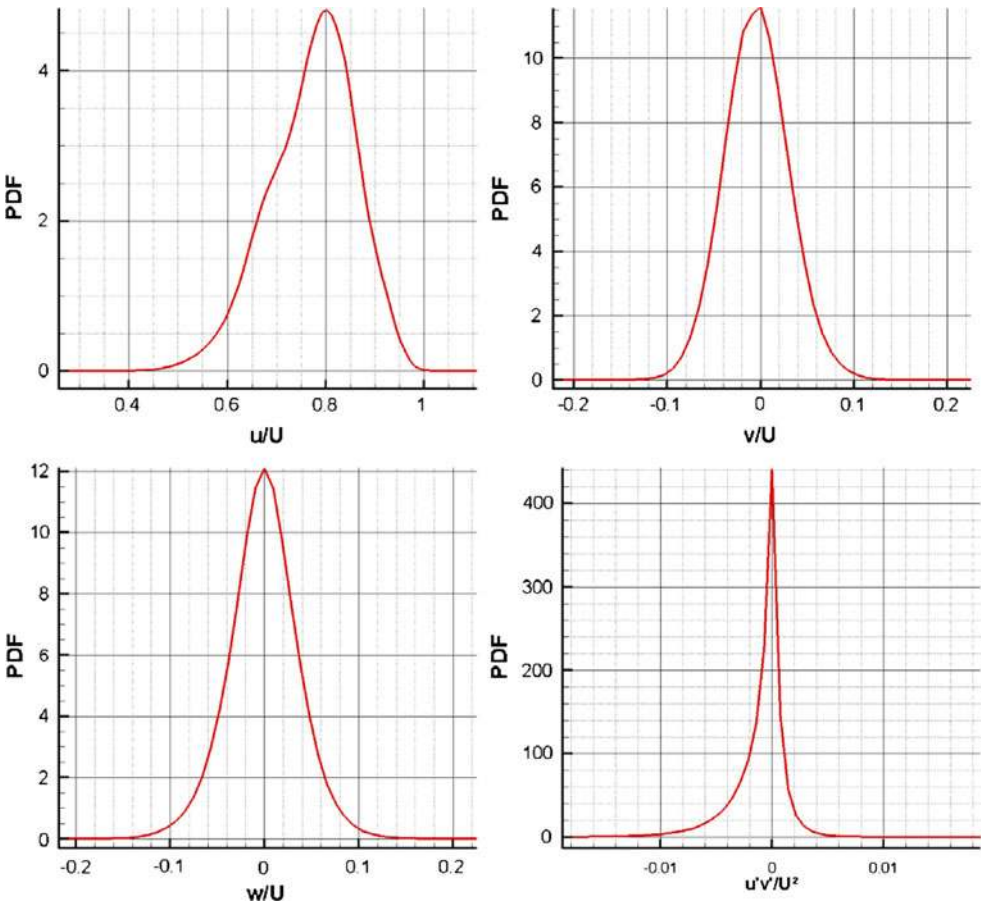

Fig. 5 PDF with band width of 0.005 m/s for u (*upper-left*), v (*upper-right*), w (*lower-left*) and a band width of 0.0002 m^2/s^2 for $u'v'$ (*lower-right*) calculated for the entire measurement volume over 5100 samples related to $U = 0.53$ m/s

do not originate from peak-locking effects, which would be sub-voxel errors of the tomographic reconstruction from several camera viewings and be visible in more locally pronounced peaks. There are lower u values visible in the PDF due to high negative u' values present in typical events (like hairpin vortices) mostly embedded in confined low-momentum structures. Additionally at around 0.35 m/s, a distinct shoulder can be observed, representing the average low-momentum streaky region, also visible in the single instantaneous vector fields. Medium higher positive u events are more often than medium lower ones as the broader high-momentum regions are less intense. There is a connection between these streaky u-formations and the presence of negative and positive v, especially closer to the wall, see e.g. two-point correlations from Ganapathisubramani et al. (2005). The v distribution in Fig. 5 (upper-right) has a broader negative part that consists of many "ejections" corresponding to the inclined arch and cane vortices coupled with low-momentum negative u' fluid and averaged over the present log-layer domain. For a comparison of the PDFs of the single-velocity components, see also the work of Herpin et al. (2008), who used high-resolution SPIV in a TBL at $Re_\theta = 2{,}200$. The PDF of the w component is almost symmetric as it should be for a statistically converged 2D flow. The PDF of the instantaneous *fluctuating* Reynolds stresses $u'v'$ shows the characteristic skewness towards the turbulence production terms; the negative $u'v'$ consist of strong Q2- and Q4-events, while Q1- and Q3-events are less intense. The maximum of the $u'v'$ distribution is exact at zero due to the high probability that values of either u' or v' are at or close to zero when using locally converged averages for Reynolds decomposition.

3.4 3D space–time correlations of the velocity components

A way to produce a more general analysis of coherent structures is the calculation of the 3D space–time correlation functions for the three velocity fluctuations u',v' and w' (Eq. 1, e.g. for u'), which provide additional statistical information on the micro- and macro scales of the averaged structures. The correlation coefficient R_{uu} at a constant wall distance y_0 is defined exemplary as:

$$R_{uu}(y_0,\Delta x,\Delta y,\Delta z,\Delta t) = \frac{\sum_x \sum_z \sum_t u\prime(x,y_0,z,t)\cdot u\prime(x+\Delta x,y_0+\Delta y,z+\Delta z,t+\Delta t)}{\sqrt{\sum_x \sum_z \sum_t u\prime^2(x,y_0,z,t)}\cdot\sqrt{\sum_x \sum_z \sum_t u\prime^2(x+\Delta x,y_0+\Delta y,z+\Delta z,t+\Delta t)}} \quad (1)$$

In Fig. 6, the results of 3D two-point space–time correlation functions R_{uu}, R_{vv} and R_{ww} named as correlation_

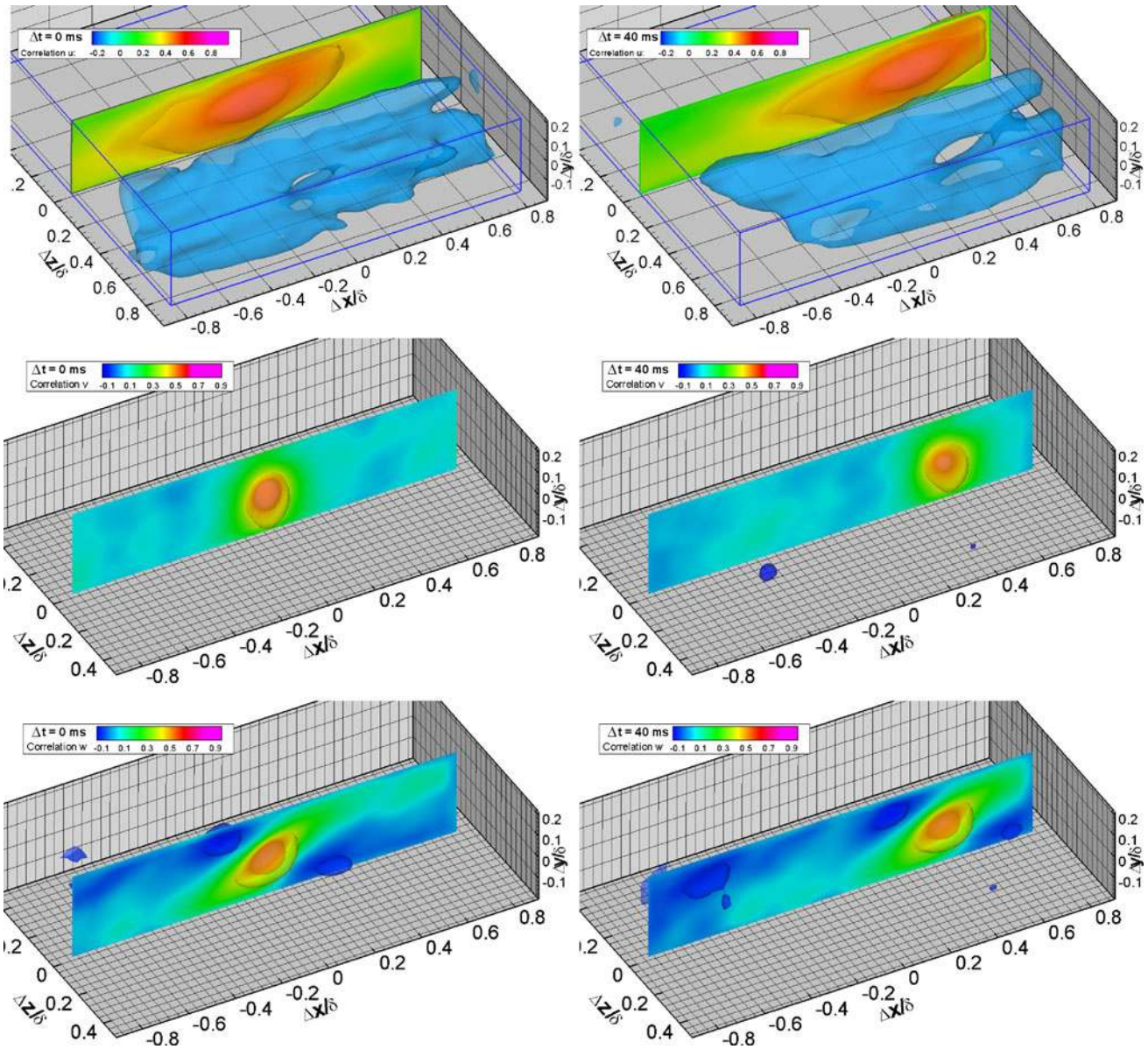

Fig. 6 3D space–time correlation functions with surface contour values of -0.2 at R_{uu}, -0.1 at R_{vv} and R_{ww} and 0.4 and 0.6 for all. A negative correlation maximum is visible for R_{uu} at $\Delta z \sim 0.5\delta$ or $\Delta z^+ = 415$ in spanwise direction (*upper*). R_{vv} (*middle*) and R_{ww} (*lower*). All R_{ij} calculated at $y = 7.45$ mm or $y_0^+ = 163$ for $\Delta t = 0$ ms (*left*) and $\Delta t = 40$ ms (*right*)

u, -_v and -_w in the figure legend is shown for two different temporal separations ($\Delta t = 0$ ms and $\Delta t = 40$ ms) at $y_0^+ = 163$ in wall normal position. The correlation function is visualized by iso-surfaces of the correlation coefficient in the normalized range $R_{ij} = [-1; 1]$. Due to the strong time dependence of the velocity vector volumes, the average has not smoothly converged over the 5,100 samples, this being especially apparent for the result at the lower correlation coefficient values. However, for R_{uu}, one can see the form of the positive correlation area, which is stretched in streamwise directions extending to $\sim$850 WU at a coefficient of 0.4, when projecting the downstream tip and upstream end onto the x-axis. The length parallel to the x-axis is consistent with Ganapathisubramani et al. (2005), who found a similar extension of R_{uu} at this value in a plane closer to the wall. A negative correlation region appears at $\Delta z \sim 0.5\delta$ corresponding to the streamwise streaky formations. The spanwise wavelength in the flow according to long streaky flow formations in log-layer regions has been quantified in good correspondence to the present data to $\sim 1\delta$ by Schlatter et al. (2010). On the other hand, the coherence in time is quite remarkable for R_{uu} and

R_{ww}, as after $\Delta t = 40$ ms, the average structure has been convected almost $\Delta x/\delta = 0.42$ downstream with only a slight narrowing mainly due to meandering motion within the flow (see Fig. 6 upper and lower). For R_{vv}, a stronger decay can be seen within the same time shift.

A remarkable extension of the upstream end at slightly increased wall distance of R_{uu} at $\Delta t = 40$ ms can be identified, which might indicate the upstream elongation of low-momentum fluid in time due to new developments of hairpin-like vortices. The increased wall distance of the elongation might be related to the differences in convection velocities to the local mean especially in long low-speed streaks (see also explanation of R_{vv} form). The measurement volume in streamwise directions is $x^+ = 1{,}380$ WU or 1.65δ, so that the correlation domain is slightly limited in x-direction according to Ganapathisubramani et al. (2005) assuming x^+ values for the streamwise integral length scale for u' at $y^+ = 92$ up to 1,500. The positive part of R_{uu} points downwards to the wall in upstream direction and upwards in downstream direction with an inclination of roughly $\sim 10°$, $-11°$ (confirming results of e.g. Foucaut et al. (2010), Zhou et al. (1999)), indicating that at the downstream tip of such streaks, there is either lower momentum over higher momentum fluid for low-speed streaks or vice versa for the tip of high-speed streaks. This phenomenon can be explained by the history of hairpin-like vortices above and along the low-speed streak forming a similar inclination angle of 12–13° found by Christensen and Adrian (2001), see also Adrian (2007), where at the downstream end separated heads convect further downstream at higher wall distances. For high-speed streaks, this characteristic could be caused by the blockage of a near-wall flow located downstream (see stagnation points found in Tomkins and Adrian (2003)), where the high-momentum fluid can only move upwards or sideways. A space correlation separated in positive and negative u' and v' for achieving their phase relations in a turbulent spot reported by Schröder (2001) showed that if there is a negative u', then the probability for a positive v' is equal in down- and upstream directions (along a low-speed streak), but if there is a positive u', then a negative v' is of high probability only upstream of that event. This is confirmed by the results of the conditional averaging in the present data shown in the chapter 3.6. R_{vv} was found to be an ellipsoid, which is stretched one-sided towards the wall, while it is narrower in spanwise than in streamwise directions. This characteristic refers to the localized wall normal fluid motion found especially in Q2 (and with less intensities in broader areas in Q4-) events with slight elongation along the u' streaks. A slight backward tilt of R_{vv} after $\Delta t = 40$ ms might be explained by the differences in convection velocities for v' especially induced by the vortical topologies around Q2 events at different wall normal positions: At the position of high v', the deficit relative to local mean is largest. For R_{ww} (Fig. 6 right), an interesting three-dimensional feature can be detected. For any spanwise velocity fluctuation present, an inclined positive correlation function at approximately 40° to the wall can be seen at $\Delta t = 0$ ms, while two negative correlation regions indicating opposite spanwise flow are present in an inclined connection line of $\sim 150°$ to the wall, one close to the wall in downstream and one further away from the wall in upstream direction. This can only be explained by the presence of inclined cane or hairpin-like vortex legs, although the spanwise flow organization has a slightly smaller inclination angle as the one of the vortices, which have been reported to be in the order of 45°–50° in this region of the TBL e.g. by Stanislas et al. (2008), Gao et al. (2010). A slightly inclined and elongated low positive correlation area at $\sim \Delta x/\delta = 0.6$ downstream and further away from the wall may indicate a matured precursor vortex with lower tilting angles as reported by Adrian (2007). Another interesting part in the same sense is visible in R_{ww} at $\Delta t = 40$ ms (Fig. 6 lower-right), where a following structure of almost the same spatial distribution of positive and negative correlation coefficients is visible further upstream. Although the low correlation values need to be inspected critically due to convergence problems, this might confirm the upstream effect and follow-up creation of hairpin-like vortices, which is quite probably along a low-speed streak, also reported by Adrian (2007)). All shapes of the auto-correlation functions are confirming findings in the literature (e.g. Kähler (2004), Ganapathisubramani et al. (2005), Foucaut et al. (2010)).

3.5 Validity check of Taylor's hypothesis

The present time-resolved 3D velocity vector data set has been used for a simple first step of a quantitative investigation of the validity of Taylor's hypothesis (Taylor (1938)) locally for all measured wall distances of the given flow. In Taylor's postulate, also known as "frozen turbulence hypothesis", it is assumed that local flow structures within a turbulent flow do not change significantly within certain time limits while convecting downstream. A sketch of the problems occurring in relation to deviating convection velocities from the mean especially for larger eddy sizes is drawn in the introduction (see also Krogstad et al. (1998) and del Alamo and Jiménez (2009)). In order to quantify the relative time limits for this TBL flow statistically, a two-point correlation R_{ij} of the time series of instantaneous velocity vector volumes with the corresponding volumes reconstructed by using Taylor's hypothesis based on local mean as convection velocities was calculated. Local mean was accepted to be very close to the convection velocities calculated by space–time

correlations at Dennis and Nickels (2008). From one vector grid plane perpendicular to the mean flow, the velocity vector volumes were reconstructed for nearly 5,000 time steps dependent on the wall distance y and averaged over the span of our measurement volume. A linear interpolation scheme has been applied in order to recalculate the vectors on the same equidistant grid as the measured ones. The reconstructed vector volumes were then compared with the actual measurement results for many (increasing) time steps; this was done by calculating the two-point correlation coefficient between the reconstructed and measured velocity fields for all three components of velocity. The slopes of correlation coefficients for R_{uu} and R_{ww} in dependence of the wall distance are shown in Fig. 7.

Noise from the limited accuracy of peak detection is always present in PIV data. In the tomo PIV case, the noise level is dependent on the direction in space according to the camera viewing set-up relative to the flow direction, so that the three-velocity components may have different evaluation noise levels. This systematic error is visible in the slight drop of the two-point correlation function from the first (autocorrelation plane with $R_{ij} = 1.0$) to the second vector grid plane ($R_{ij} \sim 0.8$–0.95), which is only 0.687 mm downstream or shifted by roughly $\sim$2 ms convection time depending on y. The further decrease in the correlation function in time is independent of this systematic error and reflects the physical de-correlation due to meandering flow motion, eddy scale dependencies of convection velocity (Krogstad et al. (1998)) and Lagrangian turbulent fluctuations, which is dependent on the wall distance and the component of velocity as expected. The only additional non-physical inhomogeneity of noise reducing the values of the two-point correlation functions, which have been averaged over the entire span in Fig. 7 left and right, is due to the increasing number of ghost particles towards the upper and lower border of the measurement volume. The corresponding kink in the iso-lines of the correlation functions is evident at the upper border at around $y^+ = 300$ and by the strong decrease in the correlation values close to the wall. But also here the decreasing slope of the correlation function with increasing time shifts is independent along the mean flow direction as the local curvatures stay stable. Additional to the correlation coefficient, iso-lines depending on streamwise distance, iso-lines of constant convection time according to the local mean velocity are added to the graphs in order to represent the different time scales of decreasing correlation for the two components of velocity across the wall-normal direction.

For the present TBL flow, the validity of Taylor's hypothesis according to R_{uu} at a wall distance of $y^+ = 150$ drops to a statistical value of 0.6 after 120 ms convection time, which corresponds to only 4 ($\sim$8 assuming underestimation) times τ_η and down to less than 0.4 for the same conditions for the w-component of velocity (see Fig. 7). This difference in decay between u and w is reflecting the respective coherence lengths in space and time (see Fig. 6). During these 120 ms, the flow structures travel along a distance of approximately 1.4 times δ. On this basis, it must be remembered that for hot-wire or LDA measurements, the calculation of e.g. flow structure sizes based on Taylor's hypothesis must be restricted to small-time intervals if the errors are not to become too large. A similar

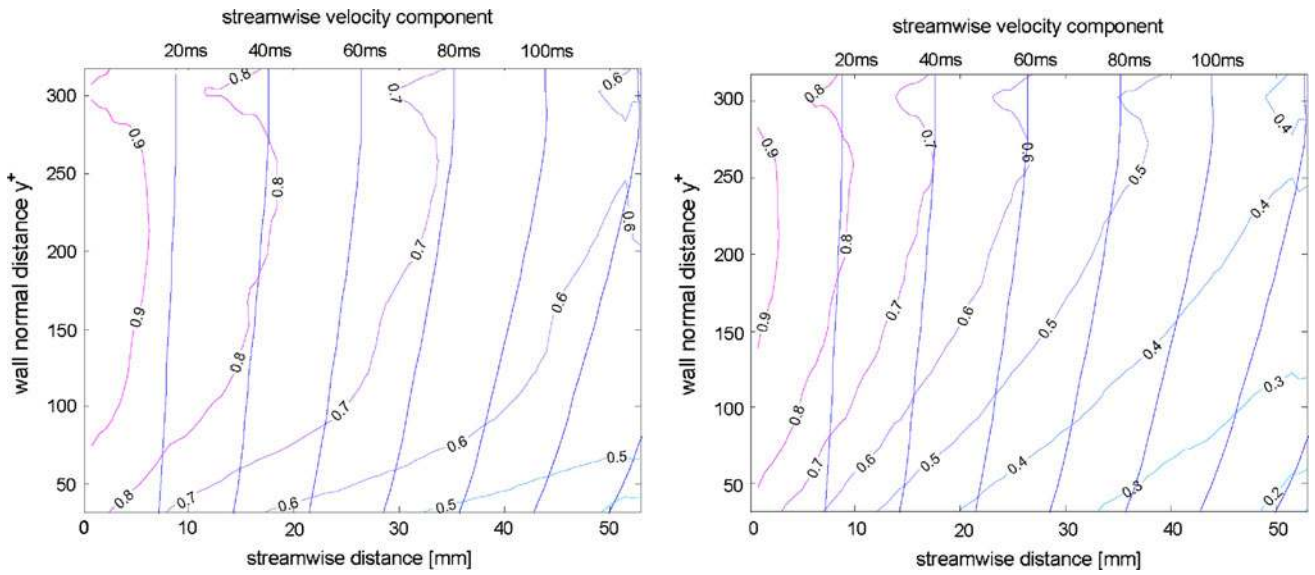

Fig. 7 Two-point correlation coefficient iso-lines with indicated correlation values of R_{uu} (*left*) and R_{ww} (*right*) of a time series of instantaneous measured and reconstructed 3D velocity vector volumes using local mean after Taylor. Reference plane (zero time shift) at $x = 32$ mm. Local average convection iso-time-lines in *blue*

investigation at only one wall distance (0.16 δ, $\sim y^+ = 240$) and a higher $Re_\theta = 4{,}685$ based on planar time-resolved PIV data has been performed by Dennis and Nickels (2008). Although our data show better correlation values for the first (noise induced) vector grid step, a stronger decay of the two-point correlation function with relative convection distance and time is visible in our data for all measured wall distances. This leads to even lower values for the validity of Taylor's hypothesis than given by the above-mentioned paper. The reason for these differences needs to be clarified especially regarding the higher Reynolds number investigated by them.

The 3D character of the flow is a key for understanding the reasons of the confinement of Taylor's hypothesis: besides the (relatively small) turbulent fluctuations decomposing an eddy when convecting downstream and the above-mentioned deviation of the convection velocity from the local mean for large coherent eddies, the main reason for the decaying slope of the correlation function seems to be the spanwise meandering nature and wall normal evolution along the flow structure trajectories inside the TBL flow, which is visible in the present time series of instantaneous velocity vector volumes (see also Hutchins and Marusic (2007) or Elsinga (2008)). Unfortunately, these arbitrary trajectories cannot be reconstructed with Taylor's hypothesis based on local average convection velocity. But also for a classical two-point space correlation based on instantaneous velocity vector volumes, the shape and size of the function is regulated by the spanwise meandering and wall-normal movements of the corresponding eddies.

3.6 Time evolution of conditional averages

One question in wall-bounded turbulence is the topological relation of negative Reynolds stress (Q2 and Q4) events and vortex structures, since hairpin-like vortices are known as organiser or at least as neighbours of such wall normal fluid exchange mechanisms see e.g. resume from Adrian (2007), Elsinga et al. (2007), Stanislas et al. (2008), or Gao et al. (2010). For a proof of the existing topology concepts of these vortices, their development and connection with the turbulence production, namely the Q2- and Q4-events, time-dependent conditional averaging was employed over the whole present dataset. Therefore, a detection and segmentation algorithm was developed. It first searches for values above a certain threshold and secondly requires a certain number of neighbours (here a minimum of 9) within the area above that threshold. Then a sufficiently large 3D box with all instantaneous velocity vectors around that event detected at a distinct wall distance (here $y = 6.87$ mm corresp. to $y^+ = 150$) was created and cut out of the single instantaneous velocity vector volumes. All boxes around all such found events in 5,100 samples were then averaged in order to obtain a smooth generic topology around the chosen event. Negative and positive time shifts of the same box and a correspondent space shift in x-direction by a distance of the local convection velocity divided by the time shift under investigation enables the calculation of precursor and successor average topologies. This enables to follow the development of the averaged structure organization around e.g. single components of vorticity and Q2- and Q4-events in the investigated log layer. Due to resolution restrictions, all near-wall vortices $y^+ < 60$ are excluded from the present investigation, so that the complete conditional history of a hairpin-like vortex development cannot be reconstructed concerning the first fluid motions at the near-wall low-speed streaks. Nevertheless, here we try a time-dependent conditional approach for the sufficiently resolved log layer assuming self-similarity of the structure development for topological interpretation.

Fig. 8 Generic 3D topology from conditional averaging of the negative y-vorticity event at $y^+ = 150$ and $t = 0$ ms and time and x-shifting of the box with respect to local convection velocity depicting flow structures by iso- surfaces of y- and x-vorticity and one velocity plane (y-velocity colour coded, *black arrow* indicates mean flow direction) ▶

We consider first the role of the *negative signed* y-vorticity for the wall normal fluid transport process without loss of generality in order to overcome symmetrization effects. A time evolution of the conditional averaged negative y-vorticity with a threshold of -0.4 ^{1}/s shows the development of a local shear type non-directional-precursor vortex at $\Delta t = -60$ ms to a $\sim 50°$ inclined and stretched vortex structure at $\Delta t = 0$ ms (time instant of event detection) in Fig. 8 (upper and middle left). This angle is confirmed also by recent work of Gao et al. (2010) using snapshot Tomo PIV in the log layer of a TBL at $Re_\tau = 2{,}400$. Further downstream at $\Delta t = +60$ ms, the detected y-vorticity tube is even more stretched with a lower inclination angle of $<40°$ and detached from the near-wall region, see Fig. 8 (lower–left). The stretching and detaching of the vortex with decreasing angle towards the wall fits to the development model of hairpin legs when the vortex head is fully developed and convects faster in a region far away from the wall above low-momentum streaks according to Adrian (2007). A second accompanying positive y-vorticity structure is present at $\Delta z^+ \sim 100$ with a much weaker maximum ($\sim 15\%$ strength) corresponding to the low probability of a symmetrical counter rotating vortex leg at the same x-position. The average spanwise distance of the two uneven conditional vortices of $\Delta z^+ \sim 100$ shows the strong dependency of the vortex generating mechanism on the wall-bounded low-speed streak size, which is also visible in this region at

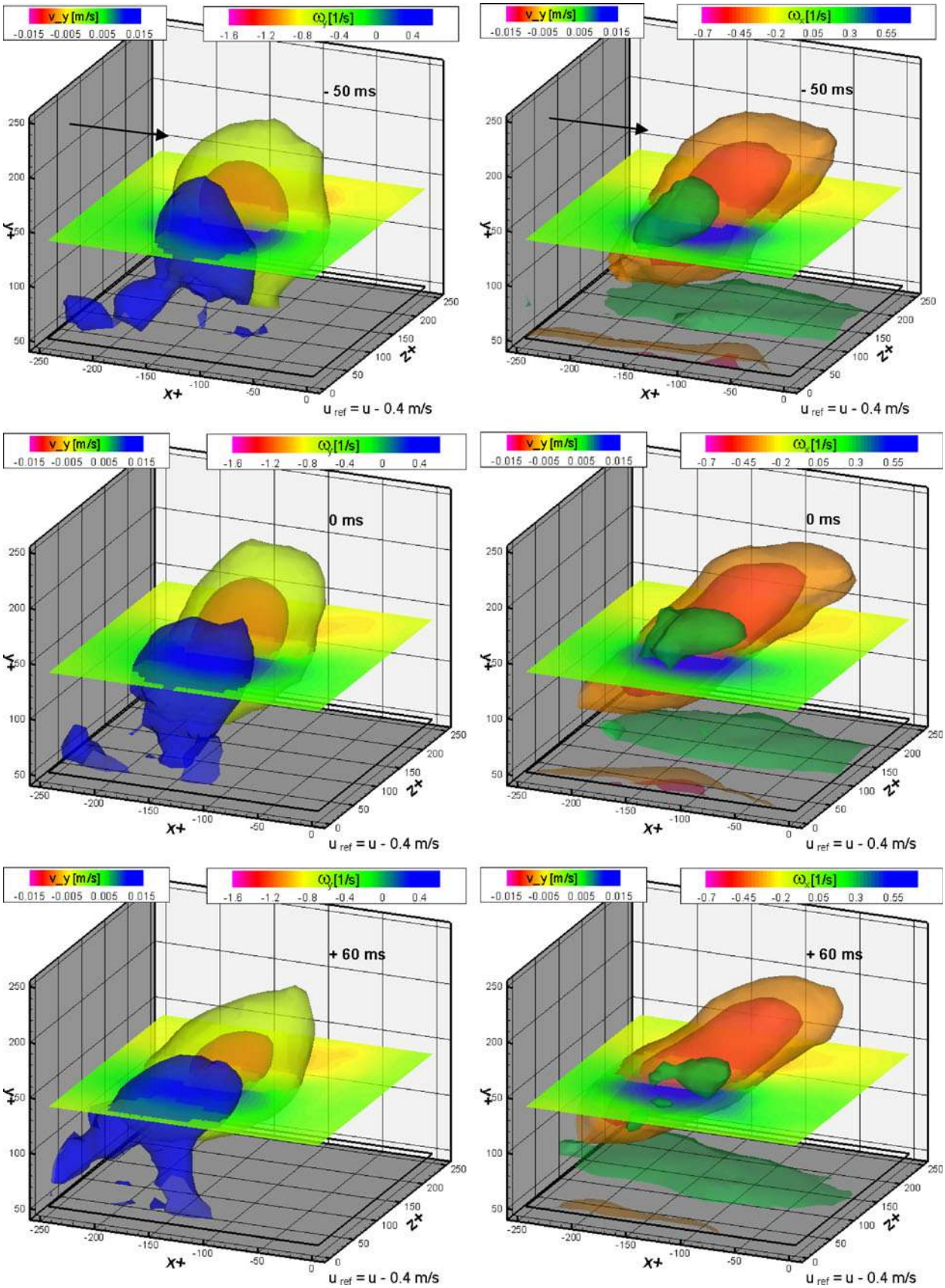
v_y [m/s]
-0.015 -0.005 0.005 0.015
ω_y [1/s]
-1.6 -1.2 -0.8 -0.4 0 0.4
- 50 ms
u_ref = u - 0.4 m/s
ω_x [1/s]
-0.7 -0.45 -0.2 0.05 0.3 0.55
0 ms
+ 60 ms
y+
x+
z+

$y^+ = 150$. This result confirms earlier findings, see resume of Adrian (2007).

On the other side, the parallel time history of x-vorticity corresponding to the conditional average of a negative y-vorticity is depicted in Fig. 8 (right column). Here, the overall values of x-vorticity are about only 2/3 of the present y-vorticity (see different colour scaling), which is also true for the corresponding Q2- and Q4-event conditional averages (x-vorticity not shown in Fig. 9) and therefore not an effect of the conditioning parameter. Note that positive x-vorticity appears at the same spanwise distance of $\Delta z^+ \sim 100$ with almost the same probability as for the y-vorticity case. The trend of the inclination angle is also a decrease within time: It develops from 45° at $\Delta t = -60$ ms, over 38° at $\Delta t = 0$ ms to 35° at $\Delta t = +60$ ms. While the differences in strength and inclination angle for the two components of vorticity at the same time instances need to be explained by its role for the wall normal fluid exchange. The inclined tube of negative x-vorticity is on the same lateral position with its maximum parallel to the region of highest wall normal motion. This picture is consistent with several earlier investigations in this wall distances using PIV in 2D mode or DNS (see Adrian (2007)). It compares well e.g. with the corresponding two-point LSE of Stanislas et al. (2008) and with an ensemble averaged structure of Guezennec (1989) in one spanwise wall normal plane both estimated closer to the wall. But the presented 3D topology and the stronger y-vorticity event at $\Delta t = -60$ ms give reasons for a slightly different interpretation of the governing dynamics of the early hairpin history than often assumed by lifting of long streamwise vortices.

3.7 Excursion: a model for the early hairpin vortex history

Presuming self-similarity of the growing mechanisms, we *firstly* assume a random high-momentum local Q4-event 'sweep' with spanwise orientation, which interacts with a low-speed streak (in accordance with Kähler (2004)). This event *secondly* produces a lift-up of low-momentum fluid with one or two local accompanying x-vorticity regions. The low-momentum fluid is than acting as an obstacle exposed to higher flow velocities producing shear and in a Kelvin–Helmholtz type of instability also local y-vorticity and *thirdly* due to the organized spanwise momentum exchange of high-momentum fluid downstream of the y-vorticity *more* wall normal fluid motion is induced: As the low-speed streak has to conserve momentum, it ejects low-momentum fluid in the first possible direction, away from wall; a self-generating local Q2 event is born. As an effect of this, *fourthly,* a locally formed inclined tube of negative x-vorticity appears. This inclination can be explained by the reason that spanwise high-momentum fluid interacts downstream of the y-vorticity causing a downstream starting point of strong wall normal fluid motion, so that the highest elevation of the x-vorticity axis is downstream of the point of highest wall normal motion. Of course all these described four processes would happen more or less simultaneously, so that a 'hen and egg' discussion might be unavoidable. In the work of Kähler (2004), basic ideas to this scenario have been developed during an analysis of fluid dynamics of wall-bounded streaks by using dual-plane stereo PIV. Nevertheless, in this interpretation, elongated streamwise vortices along low-speed streaks (not found in the data of Kähler (2004)) would not be, as often assumed, a necessary pre-requisite for an initialization of the well-described part of the hairpin-like vortex development in the log layer. Especially the fast and strong development of an 'ejection' in a local Q2-event can be traced back to the effect of a self-generating mechanism pushed by a local high-momentum Q4- event. This interpretation of the precursor dynamics of a hairpin-like leg is somewhat restricted in terms of the available precursor time of $\Delta t = -60$ ms due to the measurement volume size and, maybe even more significant, by the lack of near-wall resolution. This lack has been substituted by the corresponding data and analysis of Kähler (2004). The present interpretation should be received as a proposal for discussion. In the further development, an inclined (one-sided) vortex leg grows containing x-and y-vorticity that is guiding more high-momentum fluid spanwise towards the near-wall low-speed streaky structure, which simultaneously extends in y-direction due to the induced Q2-events. The "primary" Q4-event is supported by this vortical motion and convects with the vortex along the low-speed streak repeating the above-mentioned process in cycles. A (two-sided) arch vortex is just acting the same way on both sides of a low-speed streak. This seems to be one main reason for the relatively long lifetime of such vortices as they support the existence of laterally organized low- and high-speed streaks while guiding high-momentum fluid in spanwise direction (see w' Fig. 6 (lower)) towards the growing low-speed streak, which induces low-momentum fluid motion away from the wall. This cycle can grow and create a following similar vortex system on upstream or lateral position as described previously (see also Adrian (2007)). The low-momentum streak can grow further in streamwise and wall normal direction unless it might finally "detach" from the wall at sufficiently high Reynolds numbers (second peak in pre-multiplied cross-spectrum). End of excursion.

Fig. 9 Conditional averaged 3D velocity vector volumes over Q2 ▶ events (*left*) and Q4 events (*right*) at $y^+ = 150$ and lateral located y-vorticity iso-surfaces (*colour coded*). Subtracted convection velocities $u_{\text{ref}} = -0.35$ m/s for Q2 and $u_{\text{ref}} = -0.4$ m/s for Q4, colour coded by sign and strength

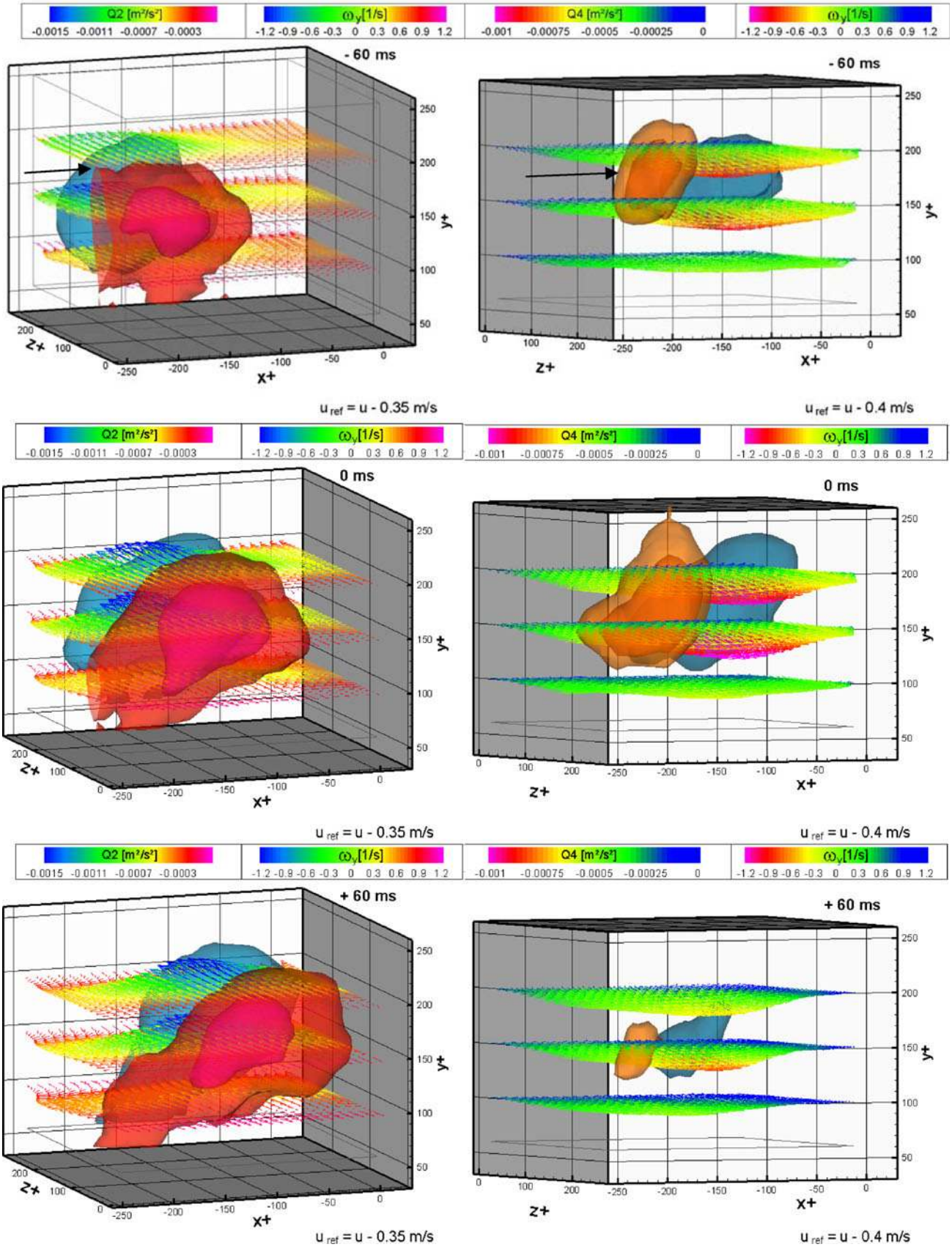
Q2 [m²/s²]
-0.0015 -0.0011 -0.0007 -0.0003
ωy[1/s]
-1.2 -0.9 -0.6 -0.3 0 0.3 0.6 0.9 1.2
Q4 [m²/s²]
-0.001 -0.00075 -0.0005 -0.00025 0
ωy[1/s]
-1.2 -0.9 -0.6 -0.3 0 0.3 0.6 0.9 1.2
- 60 ms
- 60 ms
y+
z+
x+
u ref = u - 0.35 m/s
u ref = u - 0.4 m/s
0 ms
0 ms
u ref = u - 0.35 m/s
u ref = u - 0.4 m/s
+ 60 ms
+ 60 ms
u ref = u - 0.35 m/s
u ref = u - 0.4 m/s

In Fig. 9, three boxes each of a conditional averaging of time shifted Q2- and Q4-events at $y^+ = 150$ for $\Delta t = -60$ ms, 0 ms and +60 ms relative to the detected event are depicted. These plots show the time evolution of the average velocity field, in which averaged precursor- and successor-flow structures of Q2- and Q4-events give insight into parts of the generating and decaying mechanisms. Due to the chosen condition, $u'v'$ is negative (below -0.004 m^2/s^2 for Q2 and -0.0025 m^2/s^2 for Q4), and the structures visualized by the velocity vector field in three different planes at $y^+ = [100; 150; 200]$ and by iso-contour surfaces of the y-component of vorticity show symmetry properties. Nevertheless, for the Q2-event case, a lateral growing and shifting of the maximum in wall normal direction can be observed, while the accompanying vortex structures of y-vorticity develop from a local non-directional shear-type structure (as shown in Fig. 8) at $\Delta t = -60$ ms to the well known $\sim 50°$ and later on to a $\sim 40°$ inclined vortex axis structure with increasing head size at $\Delta t = +60$ ms as described in literature. This scenario could give an additional hint for the role of hairpin-like vortices as a secondary effect of a strong shear flow and y-vorticity generation in the past as mentioned previously. After initiation of such a vortex system, it is able to self-sustain its wall normal fluid transport, while changing its shape and size as already described (see Adrian (2007)). For such threshold selected Q2-events, a lifetime of more than at least 120 ms has been found which corresponds to a convection length of more than 1.5δ. For the Q4-event case, the time evolution is quite different. Here, the precursor topologies at $\Delta t = -60$ ms indicates a flow which guides high-momentum fluid from a region further away from the wall towards it, while the related lateral vortex structures are positioned at the maximum of the Q4-event. Here, the vortex structures become also inclined from originally 50° to $\sim 40°$ within time, but loose strength while descending slightly, as well as the Q4 event itself as shown at $\Delta t = +60$ ms. The downstream effect of a high-momentum Q4-event seems to be transformed quite rapidly to other velocity components and flow structures when approaching the wall. Here, a region of strong Lagrangian accelerations and decelerations is assumed within the induced vortices and pressure fluctuations generating high shear and normal stresses produced by such a high-momentum fluid reaching the wall where low-momentum fluid is organized in relatively long time persisting streaks. The distances of the two accompanying vortices reflect the medium spanwise size of strong Q2-and Q4-events. For the Q2-accompanying vortices, a distance of $\Delta z^+ = 100$ and for the Q4-vortices, a distance of $\Delta z^+ = 120$ can be measured, which again focuses the generation process of such events to the wall-bounded low- and high-speed streaks here at $y^+ = 163$. This distance do not correspond to the medium distance of $\Delta z^+ = 415$ found between positive and negative u'-streaks in the space-correlation function at almost the same wall distance shown in Fig. 6, which can be explained by larger-scale streaks formed by packages of hairpins (e.g. Christensen and Adrian (2001) and Tomkins and Adrian (2003)).

Within the bounds given by the use of these thresholds, the average strong Q4-events are about 70% of the intensity of the average strong Q2-events. Thresholds always represent a selection mechanism, but even the use of relative thresholds is not easier to justify in anisotropic and non-homogeneous turbulence. However, for the first time, a significant time interval of a conditional-averaged hairpin vortex leg as well as of Q2- and Q4-events have been displayed for topological interpretation on the basis of temporally highly resolved volumetric tomo PIV data. Comparisons with DNS at similar Reynolds numbers require a statistically significant number of events and/or duration of time span for the numerical domain. The DNS of Schlatter et al. (2010) might fulfil these conditions.

3.8 Lagrangian views and statistics

For the detection of tracer particles in the time series of the tomographically reconstructed particle image volumes, a 3D-PTV algorithm from LaVision was employed. Sub-pixel 3D-particle locations were fitted within the volume by a $5 \times 5 \times 5$ Gaussian fit for all peaks above a 15% grey value threshold from the overall histogram. Possible particle matches were restricted by several criteria.

First, velocities must fall within a globally possible range, and the change in velocity from one time step to the next must be below an absolute value (here 2 pixel) and also less than an allowed velocity gradient ratio in pixel displacement divided by pixel distance (here 1). Finally, particles must be visible for several time steps. Given the high density of reconstructed particles with the presence of a relatively high fraction of ghost particles, only particle tracks longer than 11 time steps are used. Ambiguities arising when a particle could possibly be connected to several particles at the next time step or multiple particles be connected to the same next particle are resolved by taking the path where the particle intensity remains the most similar. Figure 10 shows selected 3D particle trajectories in a section of the investigated volume. Note that Fig. 10 depicts only a small fraction of the overall identified trajectories.

The total number of tracked particles fulfilling the above-mentioned conditions is of the order of 10^5. In order to calculate the Lagrangian accelerations, a moving cubic spline was used. For each time step, t, and around each point of a measured trajectory, a third-order polynomial was fitted from $t - 5\Delta t$ to $t + 5\Delta t$ for each component, x,

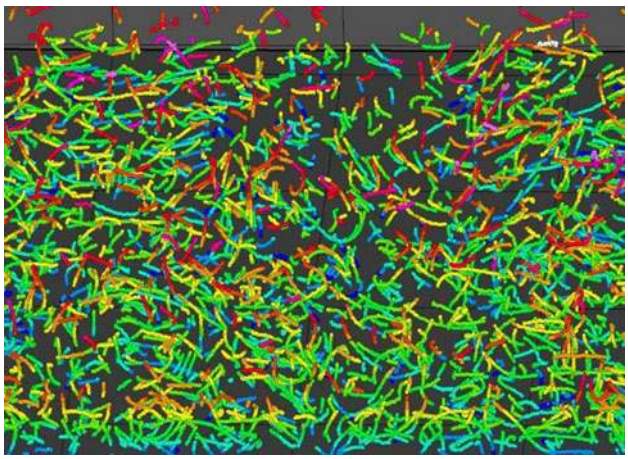

Fig. 10 Selected 3D particle trajectories in a section of the investigated volume. *Colour coding* indicates height above wall. For convenience, the displacement difference to the mean velocity (flow from *left to right*) is displayed

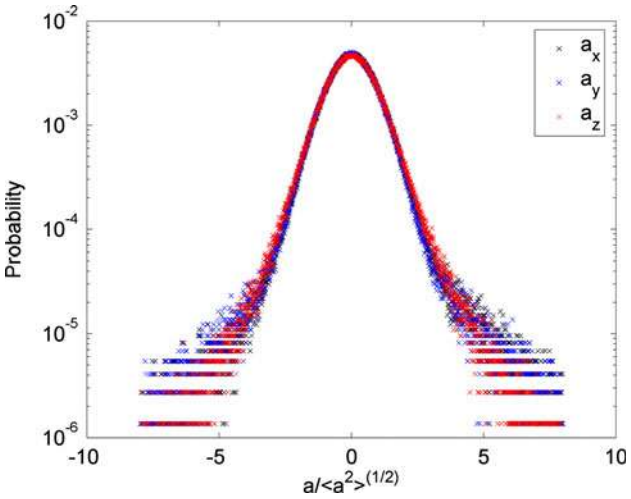

Fig. 11 Probability distribution of the Lagrangian accelerations a_x, a_y and a_z in the logarithmic layer scaled by the respective standard deviations

y, z. This results in a fit to 11 measured trajectory points. The acceleration was then derived from the second derivative of the polynomial at the respective time step (see Lüthi (2002) for more details). Figure 11 depicts the probability distribution of the single components of Lagrangian accelerations scaled by the standard deviation in x-direction between $y^+ = [30; 330]$. On a well-converged basis of $\sim 80 \times 10^6$ data points, the probability calculation shows interesting properties. As a quality check, we first compared the distributions of the Lagrangian and Eulerian velocity components from the tracking and PIV data respectively and found very good agreement in form and quantities. It can be seen that the acceleration distribution is almost symmetrical in this log-layer region confirming findings of Yeo et al. (2010). The acceleration in y-direction is slightly narrower in the middle section, but a little broader at the tails. This underlines the stronger intermittent character of a_y due to the trapping of particles in frequently appearing hairpin legs vortices, which strongly accelerates a fluid particle (according to Lee et al. (2004)) in wall normal directions on the transition from a Q4- to a Q2-event *et* vice versa). The highest acceleration values appear for all three components at the negative and positive tails (up to 8 times RMS) in an intermittent manner. The accelerations in x- and z-directions exhibit similar distributions. Gerashchenko et al. (2008) showed probability distributions of the x-direction of Lagrangian acceleration of inertial particles in a TBL at lower Reynolds numbers. The distribution for the lowest examined Stokes number of 0.035 at $y^+ = 244$ in their work are very similar to the present one, but little broader than our calculation of fluid particle accelerations shown in Fig. 11. Their distribution of accelerations in x-direction consists of normalized values up to ± 10 in the tails. However, as their work is focused on the non-intuitive finding of increasing values of Lagrangian accelerations with increasing Stokes numbers, our distribution is in good agreement with their experiment, when extrapolating down to fluid particles. In the numerical study of Yeo et al. (2010), the acceleration profiles across the boundary layer at a low Reynolds number of $Re_\tau = 180$ are presented up to $y^+ = 100$ scaled by the respective single component RMS values. The three-scaled acceleration components are of same magnitude at $y^+ > 60$ and tends to decrease further away starting from values at ~ 10 at $y^+ = 80$. Although there is a large difference in Reynolds number, the magnitudes of the present accelerations are of the same order. In a numerical study of Lavezzo et al. (2009), it was shown that RMS values of the y-acceleration of fluid particles in a turbulent channel flow tends to be slightly larger than those of the x-acceleration in regions above $y^+ = 120$, which is the main part of the investigated domain in our study. This might be the reason for the slightly narrower middle part and wider tails in the distribution of the normalized y-acceleration. On the other hand, the RMS values of x-accelerations are much larger closer to the wall and the PDF is strongly skewed for both x- and y-directions due the anisotropy very close to the wall at $y^+ < 10$ (Yeo et al. 2010). Unfortunately, all relevant investigations of Lagrangian acceleration within TBL or turbulent channel flow using either DNS (Yeo et al. 2010, Lee et al. 2004) or PTV (Gerashchenko et al. 2008) were focusing on significant lower Reynolds number and/or does not calculate the related values for the logarithmic region of the TBL. A detailed interpretation of the Lagrangian acceleration and its connection to the coherent structures detected by conditional averages goes beyond the scope of this paper, but shall be a part of further planned

investigations on this data set. As a first global result, it can be seen that the distribution of Lagrangian accelerations is slightly anisotropic, symmetric for each component (within the measurement uncertainty) and has a more intermittent character than that associated with a Gaussian distribution.

4 Conclusions

The tomographic PIV technique was applied to investigate the motion of coherent structures in a zero pressure gradient turbulent boundary layer over a flat plate in a water tunnel at $Re_\theta \sim 2{,}460$. Six high-speed CMOS cameras recorded images of small tracer particles that were illuminated by two high-repetition rate pulsed lasers in a volume of $1.65\delta \times 0.4\delta \times 1.79\delta$ at 1 kHz. Each of two subsequently acquired and reconstructed particle image distributions were cross-correlated in small interrogation volumes using iterative multi-grid schemes with volume deformation in order to determine a time series of instantaneous 3D–3C velocity vector fields with 1 kHz sampling rate.

The set of measured series of 4D instantaneous velocity vector volumes gives valuable insight into the complete flow topologies within the log layer of the TBL. Consistent and frequently appearing flow structures can be identified and related to the known models (arch- or hairpin-like vortices, streaks etc.). Time-dependent conditional averaging over certain flow events found inside the 3D velocity volumes provides a model of the connection of the turbulence producing Q2- and Q4-events and vortices in a spatial and temporal flow topology. The fluctuation components, vorticity, Reynolds stress events and the elements of the velocity gradient tensor have been time–space correlated over the whole measurement volume and shown partly. Furthermore, a simple validity check on Taylor's hypothesis was carried out on the basis of two-point correlation functions. Additionally, the PDFs of Lagrangian accelerations were computed as a first result within a moving frame of reference. Further analysis and assessment of the measurement data may contribute to the understanding of self-organization processes of the flow structures, scaling properties and momentum transfer of wall-bounded turbulent flows in the near future. A new reconstruction, evaluation and analysis of the present data set is intended combining recently developed algorithms using local Optical Transfer Functions (Schanz et al. 2010) and Motion Tracking Enhancement (Novara et al. 2010) in order to increase the accuracy of the reconstructed particle positions, the correlation quality and the spatial resolution. In future, the technique of time-resolved tomographic PIV might be transformed stepwise to a sophisticated PTV technique enabling the measurement of particle trajectories with a high spatial resolution.

Acknowledgments The authors wish to thank Prof. Dr. I. Marusic for providing the hot-wire cross- spectra.

References

Adrian RJ (2007) Hairpin vortex organization in wall turbulence. Phys Fluids 19:041301

Choi J-I, Yeo K, Lee C (2004) Lagrangian statistics in turbulent channel flow. Phys Fluids 16(3):779–793

Christensen KT, Adrian RJ (2001) Statistical evidence of hairpin vortex packets in wall turbulence. J Fluid Mech 431:433–443

Clauser FH (1956) The turbulent boundary layer. Adv Appl Mech IV, 1–51

del Alamo JC, Jiménez PZ (2009) Estimation of turbulent convection velocities and corrections to Taylor's approximation. J Fluid Mech 640:5–26

del Alamo JC, Jiménez PZ, Zandonade P, Moser RD (2006) Self-similar vortex clusters in the turbulent logarithmic region. J Fluid Mech 561:329–358

Dennis DJC, Nickels BT (2008) On the limitations of Taylor's hypothesis in constructing long structures in a turbulent boundary layer. J Fluid Mech 614:197–206

Diorio J, Douglas HK, Wallace JM (2007) The spatial relationships between dissipation and production rates and vertical structures in turbulent boundary and mixing layers. Phys Fluids 19:035–101

Elsinga GE (2008) Tomographic particle image velocimetry and its application to turbulent boundary layers. Ph.D. dissertation, Delft University of Technology (http://repository.tudelft.nl/file/1003861/379883)

Elsinga GE, Marusic I (2010) Topology and lifetimes of flow topology in a turbulent boundary layer. Phys Fluids 22:015102

Elsinga GE, Westerweel J (2010) Tomographic-PIV measurement of the flow around a zigzag boundary layer trip, p1592. In: Proceedings of 15th international symposium on applications of laser techniques to fluid Mechanics, Lisbon, Portugal, 05–08 July, 2010

Elsinga GE, Scarano F, Wieneke B, van Oudheusden BW (2006) Tomographic particle image velocimetry. Exp Fluids 41: 933–947(15)

Elsinga GE, Kuik DJ, Oudheusden BW, Scarano F (2007) Investigation of the three-dimensional coherent structures in a turbulent boundary layer with Tomographic-PIV, *AIAA 2007–1305*; 45th AIAA aerospace sciences meeting and exhibit, 8–11 January 2007, Reno, Nevada

Elsinga GE, Westerweel J, Scarano F, Novara M (2010) On the velocity of ghost particles and the bias errors in Tomographic-PIV. Exp Fluids, doi:10.1007/s00348-010-0930-0

Foucaut J-M, Coudert S, Stanislas M, Delville J (2010) Full 3D correlation tensor computed from double field stereoscopic PIV in a high Reynolds number turbulent boundary layer. Exp Fluids, doi:10.2007/s00348-010-0928-7, Online July 15, 2010

Ganapathisubramani B, Longmire EK, Marusic I (2003) Characteristics of vortex packets in turbulent boundary layers. J Fluid Mech 478:35–46

Ganapathisubramani B, Hutchins N, Hambleton WT, Longmire EK, Marusic I (2005) Investigation of large-scale coherence in a turbulent boundary layer using two-point correlations. J Fluid Mech 524:57–80

Gao Q, Ortiz-Duenas C, Longmire EK (2010) Eddy structure in turbulent boundary layers based on tomographic PIV, p1757. In: Proceedings of 15th international symposium on applications of laser techniques to fluid mechanics, Lisbon, Portugal, 05–08 July 2010

Gerashchenko NS, Sharp S, Neuscamman S, Warhaft Z (2008) Lagrangian measurements of inertial particle accelerations in a turbulent boundary layer. J Fluid Mech 617:255–281

Guezennec YG (1989) Stochastic estimation of coherent structures in turbulent boundary layers. Phys Fluids A 1, 1054 (1989). doi: 10.1063/1.857396

Hambleton WT, Hutchins N, Marusic I (2006) Simultaneous orthogonal-plane particle image velocimetry measurements in a turbulent boundary layer. J Fluid Mech 560:53–64

Herpin S, Wong CY, Stanislas M, Soria J (2008) Stereoscopic PIV measurements of a turbulent boundary layer with a large spatial dynamic range. Exp Fluids 45:745–763

Hutchins N, Marusic I (2007) Evidence of very long meandering features in the logarithmic region of turbulent boundary layers. J Fluid Mech 579:1–28

Kähler CJ (2004) The significance of coherent flow structures for the turbulent mixing in wall-bounded flows, Dissertation, DLR Forschungsbericht 2004 -24, ISSN 1434-8454, or online publication at http://webdoc.sub.gwdg.de/diss/2004/kaehler/kaehler.pdf

Krogstad P-Å, Kaspersen JH, Rimestad S (1998) Convection velocities in a turbulent boundary layer. Phys Fluids 10(4): 949–957

Lavezzo V, Soldati A, Gerashchenko S, Warhaft Z, Collins L (2009) Direct Numerical Simulation of inertial particle accelerations in near-wall turbulence: comparison with experiments. Webpaper: www.aidic.it/icheap9/webpapers/306Lavezzo.pdf

Lee C, Yeo K, Choi J-I (2004) Intermittent nature of acceleration in near wall turbulence. Phys Rev Let 92:144502

Lüthi B (2002) Some aspects of strain, vorticity and material element dynamics as measured with 3D Particle Tracking Velocimetry in a Turbulent Flow. Dissertation

Marusic I, McKeon BJ, Monkewitz PA, Nagib HM, Smits AJ, Sreenivasan KR (2010) Wall-bounded turbulent flows at high Reynolds numbers: recent advances and key issues. Phys Fluids 22:065103

Moin P (2009) Revisiting Taylor's hypothesis. J Fluid Mech 640:1–4

Mordant N, Lévèque E, Pinton J-F (2009) Experimental and numerical study of the Lagrangian dynamics of high Reynolds turbulence. Submitted to Phys Fluids

Nickels T, Marusic I (2001) On the different contributions of coherent structures to the spectra of a turbulent round jet and a turbulent boundary layer. J Fluid Mech 448:367–385

Novara M, Batenburg KJ, Scarano F (2010) Motion tracking-enhanced MART for tomographic PIV. Meas Sci Technol 21:035401

Robinson SK (1991) The kinematics of turbulent boundary layer structure. NASA Technical Memorandum, 103859

Saikrishnan N, Marusic I, Longmire EK (2006) Assessment of dual plane PIV measurements in wall turbulence using DNS data. Exp Fluids 41:265–278

Scarano F, Poelma C (2009) Three-dimensional vorticity patterns of cylinder wakes. Exp Fluids 47:69–83

Schanz D, Gesemann S, Schröder A, Wieneke B, Michaelis D (2010) Tomographic reconstruction with non-uniform optical transfer functions (OTF). In: Proceedings of 15th international symposium on applications of laser techniques to fluid mechanics, Lisbon, Portugal, 05-08 July, 2010, p 1709

Schlatter P (2010) Vortical and large-scale structures in a turbulent boundary layer, Poster, Linné FLOW Centre, KTH Mechanics, Stockholm, Sweden, http://www.mech.kth.se/~pschlatt/DATA/README.html

Schlatter P, Li Q, Brethouwer G, Johansson AV, Henningson DS (2010), Simulations of spatially evolving turbulent boundary layers up to $Re_\theta = 4300$. Int J Heat Fluid Flow. doi: 10.1016/j.ijheatfluidflow.2009.12.011

Schoppa W, Hussain F (1997) Genesis and dynamics of coherent structures in near-wall turbulence. In Panton R (ed) Self-sustaining mechanisms of wall turbulence. Computational Mechanics Publications, pp 385–422

Schröder A (2001) Untersuchung der Strukturen von künstlich angeregten transitionellen Plattengrenzschichtströmungen mit Hilfe der Stereo und multiplane particle image velocimetry. http://webdoc.sub.gwdg.de/diss/2001/schroeder/schroeder.pdf

Schröder A, Kompenhans J (2004) Investigation of a turbulent spot using multi-plane stereo PIV. Exp Fluids 36:82–90 Selected issue

Schröder A, Geisler R, Elsinga GE, Scarano F, Dierksheide U (2006) Investigation of a turbulent spot using time-resolved tomographic PIV., CD-Rom. Paper 1.4. In: Proceedings of 13th international symposium on applications of laser techniques to fluid mechanics, June 26–29, Lisbon (Portugal)

Schröder A, Geisler R, Elsinga GE, Scarano F, Dierksheide U (2008) Investigation of a turbulent spot and a tripped turbulent boundary layer flow using time-resolved tomographic PIV. Exp Fluids 44(2):305–316

Spalart PR (1988) Direct simulation of a turbulent boundary layer up to $Re_\theta = 1410$. J Fluid Mech 187:61–98

Stanislas M, Perret L, Foucaut J-M (2008) Vortical structures in the turbulent boundary layer: a possible route to a universal representation. J Fluid Mech 602:327–382

Taylor GI (1938) The spectrum of turbulence. Proc R Soc Lond Ser A 164:476–490

Tomkins CD, Adrian RJ (2003) Spanwise structure and scale growth in turbulent boundary layers. J Fluid Mech 490:37–74

Virant M, Dracos T (1997) 3D PTV and its application on Lagrangian motion. Meas Sci Technol 8:1539–1552

Wieneke B (2007) Volume self-calibration for Stereo PIV and Tomographic PIV. In: Proceedings of PIV'07, Rome, 11–14 September 2007

Yeo K, Kim B-G, Lee C (2010) On the near-wall characteristics of acceleration in turbulence. J Fluid Mech. doi:10.107/S00221120100002557

Zhou J, Adrian RJ, Balachandar S, Kendall TM (1999) Mechanisms for generating coherent packets of hairpin vortices in channel flow. J Fluid Mech 387:353–396